University of Padova

Department of Physics and Astronomy "Galileo Galilei"

Master Thesis in Astrophysics And Cosmology

Quantifying the effects of an in-orbit fragmentation of space objects: an environmental index for the Space Surveillance and Tracking (SST) services

Supervisor
Prof. F. Marzari
University of Padova

Co-supervisor
Dr. A. Rossi
IFAC-CNR

Master Candidate
Luigi Gisolfi

Student ID
2057825

Academic Year
2023-2024

"Gutta cavat lapidem, consumitur anulus usu"
— Ovidio, Epistulae ex Ponto, libro IV, 10, 5.

Abstract

In the framework of the Fragmentation Service of the European SST system, it is important to quickly assess whether a fragmentation event is posing an immediate threat to the assets orbiting in close-by regions of space and if it is going to stress the capabilities of the surveillance network. The derivation of an analytically computable index, able to quantify the severity of an event under these points of view, can help the SST system to better deal with these unexpected events.

Contents

Listing of figures

Listing of tables

Listing of acronyms

TLE ..... Two-Line-Element
SSN ..... Space Surveillance Network
USSTRATCOM ... US Strategic Command
SSR ..... Satellite Situation Report
ASAT ..... Anti-Satellite
IADC ..... InterAgency Debris Coordination Committee
LEO ..... Low-Earth Orbit
MEO ..... Medium-Earth Orbit
HEO ..... High-Earth Orbit
GEO ..... Geostationary Orbit
EUSST ..... EU Space Surveillance and Tracking
CA ..... Collision Avoidance (service)
RE ..... Re-Entry (service)
FG ..... Fragmentation (service)
CAM ..... Collision Avoidance Manoeuvers
CDM ..... Conjunction Data Messages
PoC ..... Probability of Collision
CSI ..... Criticality of Spacecraft Index
SC ..... Shell Criticality
FEI ..... Fragmentation Environmental Index
MASTER ..... Meteroid and Space Debris Terrestrial Environment Reference
SDM ..... Space Debris Mitigation
IO ..... Initial Orbit
TRADEX ..... Target Resolution and Discrimination Experiment
EISCAT ..... European Incoherent Scientific Association
ESR ..... EISCAT Svalbard Radar
GRAVES ..... Grand Réseau Adapté a la Veille Spatiale
TIRA ..... Tracking and Imaging Radar
RSO ..... Resident Space Object

AR . . . . . Angular Rate

SNR . . . . . Signal to Noise Ratio

QE . . . . . Quantum Efficiency

RCS . . . . . Radar Cross Section

RAAN . . . . . Right Ascension of the Ascending Node

SSA . . . . . Space Situational Awareness

PFO . . . . . Post-Fragmentation Orbit

1 Introduction

1.1 The Issue of Space Debris

On October 4, 1957, the Soviet Union launched the Sputnik satellite in a low elliptical orbit around the Earth. It was the world's first artificial satellite, and it ushered in a new era: the Space Age had just begun. At that time there was no plan for what to do with space objects at the end of their lives. Tonnes of spacecraft, rockets and instruments have been launched to space, making it quite a crowded place. Further items, such as screwdrivers and protective gloves were also released unintentionally later on, when astronauts started performing extra-vehicular activities. It soon became clear that an understanding of the environment produced by man-made objects in orbit around the Earth was necessary for a sustainable future of spaceflight. Starting from this consideration, observations of space objects and precise orbit determination were carried out. This information contributed to the creation of the first catalogs, the most comprehensive of which is the Two-Line Element (TLE) catalog of the US Strategic Command (USSTRATCOM), based on the US Space Surveillance Network (SSN). Further information can be found in the NASA Satellite Situation Report (SSR).

Besides the objects intentionally launched to space, other events contributed to the proliferation of orbiting objects. On June 29, 1961, the first in-orbit break-up event took place. The upper stage of the Thor-Ablestar rocket employed to put the US Transit-4A satellite into orbit exploded, leaving at least 298 trackable fragments. The space traffic increased instantaneously, and new objects entered the field of view of telescopes all around the world. Some 40 years later, about 200 Ablestar fragments were still found to be orbiting the Earth (see [5]). It was the first documented fragmentation event ever registered: after that, we knew space debris was destined to become an issue. Following the intentional explosions of the first anti-satellite weapons (ASAT) and the explosions of nine Delta second stages between 1975 and 1981, scientists started addressing the problem.

In 1978, Donald J. Kessler and Burton G. Cour-Palais published the paper "Collision Frequency of Artificial Satellites: The Creation of a Debris Belt" ([6]). They predicted that, if the past growth rate in the cataloged pop-

ulation continued, the hazard coming from this new source of debris would quickly exceed the one set by natural meteoroids increasing over longer periods of time, even if a zero net input rate in the catalog was maintained. More precisely, [7] identified two types of instabilities: the first is an unstable environment, characterized by an insufficient number of fragments for the number of intact objects that exist. Over time, the number of fragments in this environment would increase until it reaches equilibrium, at which point the environment would remain stable so long as the number of intact objects remains constant. In contrast, the second kind of instability, a "runaway" environment, is characterized by the number of fragments increasing indefinitely for as long as the intact population remains unchanged.

These findings have important implications. First of all, a critical density exists under which the environment only suffers from the first type of instability: in this case, the debris population would keep on increasing, until a new equilibrium with natural forces (e.g. atmospheric drag) is reached. On the other hand, had the critical density been reached, the system would experience a runaway growth: the total amount of space debris would keep on increasing exponentially; collisions would rise to more debris and lead to more collisions, in a chain reaction process which was later termed "Kessler Syndrome" by J. Gabbard. While the fragment population in a runaway equilibrium may theoretically approach infinity, this situation could never occur because it would require replacing an infinite number of intact objects after every collision in order to maintain the constant population of intact objects. However, it is crucial to take this instability seriously because it imposes a practical limit on the number of objects that can be maintained in orbit without increasing the small debris population.

Instability of the first type is likely to be characteristic of many altitudes above 600 km - especially the ones of crowded regions around 800 km and 1000 km - since the atmospheric drag - and consequently, the sinking of fragments - becomes weaker with altitude. For instance, the crowded regions around 800 km and 1000 km are predicted to be above the unstable threshold, as well as other heavily populated high-altitude shells, such as the one around 1500 km, for which a sink of fragments is virtually non-existent.

Within this unstable scenario, a reduction in the size, number, or orbital inclination of intact objects will lead to a decrease in the number of fragments that will eventually end up in the environment, since the population of fragments is strongly related to the population of intact objects at a particular altitude. More specifically, some space debris has the potential to damage spacecraft, leading to loss of mission, or loss of life in the case of manned spacecraft. Space debris mitigation measures are therefore highly relevant during our times. For this reason, in 2002, the InterAgency Debris Coordination Committee published the IADC Space Debris Mitigation Guidelines. This served as a baseline for the UN Space Debris Mitigation Guidelines, to be considered for the mission planning, design, manufacture and operational (launch, mission, and disposal) phases of spacecraft and launch vehicle orbital stages:

- Guideline 1: Limit debris released during normal operations.
- Guideline 2: Minimize the potential for break-ups during operational phases.
- Guideline 3: Limit the probability of accidental collision in orbit.
- Guideline 4: Avoid intentional destruction and other harmful activities.
- Guideline 5: Minimize the potential for post-mission break-ups resulting from stored energy.
- Guideline 6: Limit the long-term presence of spacecraft and launch vehicle orbital stages in the Low-Earth Orbit (LEO) region after the end of their mission.

- Guideline 7: Limit the long-term interference of spacecraft and launch vehicle orbital stages with the Geosynchronous Earth Orbit (GEO) region after the end of their mission.

Since the mid-1990s, space agencies in Europe have developed more technically oriented guidelines as a European Code of Conduct, whose core elements are in line with the UN and IADC guidelines. For instance, the European Space Agency developed its own Requirements on Space Debris Mitigation for Agency Projects in 2008, superseded by the ISO standard 24113 on debris mitigation requirements. Among other things, the updated ISO standard requires:

- a probability of successful disposal of 0.90, meaning that a spacecraft must demonstrate a high probability of successful disposal, coupled with high reliability throughout its design lifetime;
- collision avoidance capability against known objects for all GEO spacecraft (for LEO spacecraft, it is required only of those that have a maneuvering capability).
- compliance with the 25-year LEO disposal rule, meaning that a spacecraft or orbital stage which cannot by design perform collision avoidance maneuvers must be removed from LEO within 25 years from the end of its operational life;
- limiting the number of debris objects released by a launch vehicle;
- limiting the ejection of slag from solid rocket motors.

Nowadays, constant monitoring of circumterrestrial space and an understanding of the events across different orbital regimes is clearly necessary to protect space-based infrastructure, facilities, and services. That's why, in 2014, the European Union established the Space Surveillance and Tracking (EUSST) support framework. This is a coordination between France, Germany, Italy, Poland, Portugal, Romania, Spain and the United Kingdom, in cooperation with the EU Satellite Center, that has the aim to mitigate the risk of damage of the assets in orbit. The EUSST provides three distinct services: 1) Collision Avoidance (CA), 2) Re-entry Analysis (RE), 3) Fragmentation Analysis (FG). In this thesis, we will mainly focus on the latter.

2

The EU Space Surveillance and Tracking

Whether it is to provide voice communication to areas where phone lines are damaged after a disaster, to see the weather on a global scale, or to count the steps we take during the day, satellites and space-based assets are an important piece of the modern world's economies and societies. It is therefore crucial to keep them safe and secure in orbit. Unfortunately, they are increasingly at risk from collision with other operational spacecraft or debris, for the reasons we mentioned in 1. Moreover, objects may re-enter the atmosphere uncontrollably, and cause damage to the ground. To protect people, infrastructures and assets, we need to be able to survey and track these space objects. The European SST was established with such goals: it allows for a risk assessment of in-orbit collisions and uncontrolled re-entry of space debris, and detection and characterization of in-orbit fragmentations. This is done by a network of sensors (e.g. radars and optical telescopes, laser ranging stations, etc) distributed worldwide (see Fig. 2.1), even if mostly on European territory, capable of surveying and tracking space objects in all orbital regimes: **Low-Earth Orbit (LEO), Medium-Earth Orbit (MEO), High-Earth Orbit (HEO) and Geostationary Orbit (GEO)**. The data collected by these ground-based assets is then analyzed and imported into a joint database, and ultimately a catalog. All of this is done by the first two of the three SST's main functions: sensor and processing. The third one - the service provision function - provides the three SST services: **Collision Avoidance (CA), Re-Entry Analysis (RE) and Fragmentation Analysis (FG)**. The French and Spanish operation centers are in charge of the Collision Avoidance service, while the Italian one takes care of the Re-Entry and Fragmentation Analysis Service. More than 130 organizations are currently receiving these services and 240+ European satellites are safeguarded from the risk of collision. We will take a detailed look at these services in the next sections.

Figure 2.1: Geographical layout of the EUSST network: radars (black), telescopes (blue) and lasers (pink). Credits: I. Urdampilleta et al. "System Approach to Analyse the Performance of the current and future EU Space Surveillance and Tracking System at Service Provision level", AMOS 2022

2.1 Collision Avoidance (CA) Service

The **CA Service** assesses the risk of collision between spacecraft and between spacecraft and space debris, generating collision avoidance alerts. Based on their associated risk, the collision events are of three types:

- **Info Events (INFOs)**: close approaches with a low associated risk;
- **Interest Events (IEs)**: close approaches with a moderate level of risk, thus requiring further analysis;
- **High-Interest Events (HIEs)**: close approaches associated with a high level of risk, potentially requiring **Collision Avoidance Manoeuvres (CAMs)**.

This CA service becomes really efficient thanks to the synergy between the Owner/Operator (O/O) and the French and Spanish Operation Center: a hot redundancy scheme is applied, with the two different OCs ready to provide the services as a single service provider. In case of need, direct dialogue can be established with the OCs, 24/7, to better understand the event.
The CA service provides three types of products: Conjunction Data Messages (CDMs), reports associated with each CDM, and monthly reports. * For all the CDMs produced, the OCs make **ephemerides analysis** and **Probability of Collision (PoC) Sensitivity analysis** available.

*A Conjunction Data Message is a standard message for use in exchanging spacecraft conjunction information between originators of collision assessments and satellite O/Os.

Among other things, the SST portal enables users to directly access CA events or download them, upload ephemerides and manoeuvre information, view the evolution of conjunctions, and direct communication with the OCs and the Front Desk.

2.2 Re-Entry Analysis (RE) Service

The **RE service** is provided by the Italian OC. It monitors all rocket bodies, specific objects of interest, and space objects with a mass greater than 2000 kg, with the goal of monitoring the re-entry into the atmosphere of artificial space objects potentially dangerous for the population and the ground structures. Concerning the above-mentioned mass limit, no mass information on the re-entering object may be available: in that case, objects with radar cross-section larger than $1m^2$ are considered. Overflight predictions provide ground tracks over customizable areas of interest, but the re-entry predictions are subject to uncertainties, and there's no guarantee that the re-entering objects will impact the specified territory. RE-entry products are associated to a risk index, related to the mass of the object. The available knowledge increases as the observations increase - allowing for better predictions as time passes by. All available information is analyzed in order to provide two products: the **30 Days Re-entry List** and the **Re-entry Report**. The former provides a list of all space objects predicted to re-enter the Earth's atmosphere in an uncontrolled manner within 30 days; the latter includes a detailed analysis focusing on the objects expected to re-enter approximately 3-4 days before the predicted re-entry epoch. This product complements the 30 Days Re-entry List by providing orbital information, ground tracks, and ground swath to confirm the final/decay report RE report, released no later than three days after the last re-entry epoch estimation, or after three no-shows by sensors contributing to EUSST.
The products are delivered through the SST Portal.

2.3 Fragmentation Analysis (FG) Service

Fragmentations in space are extremely detrimental events that might seriously jeopardize all the space assets orbiting within a specific orbital region. It is therefore of paramount importance to be able to quickly assess and characterize any such event to warn the observing network and all the interested operators of the incoming danger. The **FG service** provides detection and characterization of in-orbit fragmentations. A **Short-term FG analysis** is carried out as soon as a fragmentation event is confirmed. It provides:

- data sources (from EU SST sensors and/or external sources);
- fragmentation event characterization (event type, number of detected fragments, orbital regime);
- object(s) identification and characterization (object type, apogee/perigee of the parent object(s) at the event time)

As soon as detailed information becomes available, the **Medium-term FG analysis** provides:

- fragments distribution (e.g Gabbard diagram);

- orbital parameters dispersion of the fragments at different times;
- 3D cloud evolution of the fragments at the time of the report creation and after 1-2 months;
- 3D graph of the position of the object(s) at the event time;
- early Impact Risk Analysis for specific altitude layers including assets of interest.

Ultimately, the **Long-Term analysis** complements previous analyses. It gives information on:

- event update;
- simulations of the event using an adequate breakup/collision model;
- expected number of fragments greater than 7 cm;
- Area to Mass ratio distribution;
- Delta Velocity distribution;
- objects' spatial density evolution.

The three products of the FG service are related to the three analyses that are carried out over time: a **Short-Term, Medium-Term and Long-Term report** are provided, respectively within a few days, within three weeks and within three months after the fragmentation.
As for the other services, the delivery of the FG service between the users and the OC is carried out via the SST Portal, which enables to access the information and to receive email notifications when updated FG products are available.

3

The Development of a Fragmentation Index

In order to quickly characterize and possibly visualize the collision risk and the environmental impact of specific spacecraft in orbit, it is useful to have analytical indicators (*indexes*) that encapsulate the physical information contributing to those quantities. The **Criticality of Spacecraft Index (CSI, see [8])** and the **Shell Criticality (SC, [9])** represent two efforts in this direction, allowing to characterize and rank the environmental criticality of single objects (CSI) and the global criticality of specific regions (altitude shells) of the circumterrestrial space. Additionally, in the framework of the Fragmentation Service of the European SST system, it is important to quickly assess whether a fragmentation event is posing an immediate threat to the nearby orbiting assets, and if it is going to stress the capabilities of the surveillance network. Therefore, it is crucial to develop an analytically computable index that is ideally able to quantify the severity of an event. In turn, this can help the SST system to better deal with such unexpected events. In this context, building on the definition of the CSI and of the SC, an index able to quantify and visualize the medium-term effects on the environment of fragmentation in Low Earth Orbit has been derived in [1]. This new **Fragmentation Environmental Index (FEI)** was shown to be able to characterize the evolution of the fragment clouds and their impact on the environment around the event location. The focus of the FEI is also to highlight the impact of a given fragmentation on a specific space surveillance system. This was initially done by the authors introducing a specific weighting factor to increase the importance, in the index computation, of objects that are non-detectable from the considered network of sensors. This is done because the non-detectable objects clearly cannot be tracked and therefore cannot be avoided with a manoeuvre.

However, an identification of the best weighting factors for specific applications - and possibly the adoption of other weights beyond the one discussed in the original paper - will allow for an improvement of the index. In this thesis, we will indeed try to introduce new weighting factors, in an effort to refine the FEI definition.

3.1 The Criticality of Spacecraft Index (CSI)

Considering the space debris issue, large parametric studies of massive breakups have been conducted in the last few years. Simulations of different fragmentations in various orbital regimes allowed for ways to classify space objects in LEO. Among others, the Criticality of Spacecraft Index (CSI) as devised in [8] is a simple analytical index able to catch, also visually, the environmental criticality of abandoned objects in Low Earth Orbit (LEO). The CSI is formulated by taking into account the physical characteristics of the space object, its orbit, and the environment it occupies. This information is used to identify the severity of the risk that the object poses to other space debris or operational spacecraft. The simulations showed how the four main parameters influencing the space debris environment's long-term evolution are the following:

1. **Spatial density** of objects as a function of time and altitude (D).
   It is well known that the collision probability in regions where a higher concentration of objects is found will be higher. To get information on how the spatial density of objects varies as a function of the altitude, a simulation of the evolution of the space debris environment spanning 200 years was carried out. This considered the population of objects larger than 10 cm from the MASTER 2009 population* and was performed with SDM 4.2†. A reference scenario assuming an evolution of space traffic similar to the one observed in recent years (as described in [8]) was adopted as a starting point for the simulation. The spatial density of objects as a function of altitude for every year was then recorded and stored. Then, given a specific epoch and the orbital altitude h of the object under consideration, the spatial density $\rho(h)$ was taken from the stored values and normalized to the maximum value of spatial density in the initial year 2009, ρ_0, corresponding to an altitude of 770 km. Figure 3.1 shows the spatial density of objects larger than 10 cm as a function of the altitude, for the epochs 2009, 2059, and 2019.

2. **Lifetime** of the objects as a function of the orbital altitude (L).
   The more time an object spends in space, the more likely it is that it will be destroyed by a collision. At low altitudes, the **atmospheric drag**, caused by the impact of the spacecraft against the molecules of the residual atmosphere, subtracts energy from the orbit and causes a secular decrease of the semimajor axis thus lowering the lifetime of an object. Therefore it contributes to lowering the cumulative threat posed by an object. This is a natural *sink factor* for space debris: any object in low-Earth orbit (below approximately 900-1000 km of altitude) will eventually re-enter the Earth's atmosphere, and it will do so after a time L which is a function of the orbital altitude h, $L(h)$. Specifically, the **lifetime** curve of a typical object in

*The Meteoroid and Space Debris Terrestrial Environment Reference (MASTER) is the European Space Agency reference population of orbiting objects. Developed by means of an event-based simulation that reproduces all the past launches, explosions, and collisions, it creates a synthetic population of orbiting objects, from large intact spacecraft down to micron-size fragments. The obtained objects are then propagated to a common reference epoch and stored in a large database. A suite of accompanying software allows the processing of the orbital information to obtain quantities such as fluxes, collision probabilities etc.

†Space Debris Mitigation (SDM) is a space debris long-term analysis program developed by [10]. It has been designed to analyze the evolution of the space debris environment and assess the effectiveness of mitigation measures. It integrates the objects in the initial debris population by means of an accurate orbital propagator accounting for all the main gravitational and non-gravitational perturbations. It considers all the main source (e.g., launches, explosions, collisions,...) and sink (e.g., atmospheric drag) mechanisms responsible for the production or removal of objects from space. The resulting orbital population can be used to compute a number of output quantities, such as the collision probability among the objects, the spatial density of objects in different regions, the number of collisions, etc.

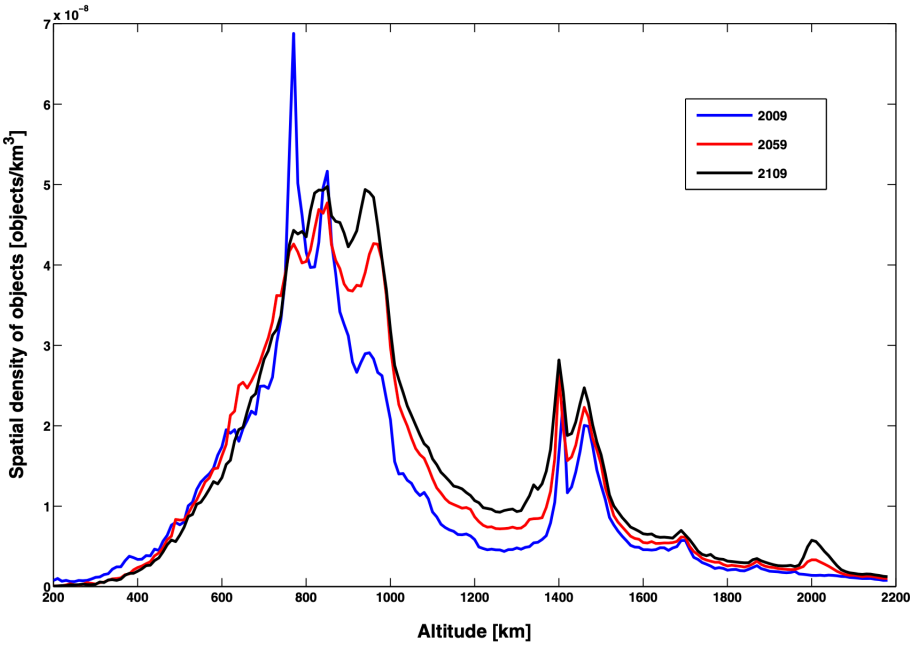

Figure 3.1: Spatial density of objects as a function of altitude for the epochs 2009 (blue line), 2059 (red line), and 2109 (black line).

LEO can be fitted by the power law:

$$log(L(h)) = ah^b + c, \tag{3.1}$$

where $a = 14.18$, $b = 0.1831$, c = -42.94 are the coefficients of the fit. Therefore, the lower altitude objects can be classified as less dangerous to the environment, their lifetime being lower. On the other hand, due to the exponential decay of the atmospheric density with altitude, the cleaning action of the atmosphere becomes inefficient at high altitudes. Figure 3.2 shows the power law fit (and the associated residuals of the fit) for a sample object with an area over mass ratio (A/M) typical for an intact spacecraft (it is worth stressing that the drag perturbation is dependent from the ratio A/M of an object, i.e. lightweight objects with large cross sections tend to decay much faster than compact heavy objects). Please note that, already at an altitude of $h = 700$ km, the lifetime of an object is expected to be of the order of 100 years, thus *de-facto* limiting the "cleaning" effect of the atmosphere to a restricted altitude band.

3. **Mass** of the objects (M).
   A more massive object will produce more fragments once destroyed following a collision.

4. **Inclination** of the objects (i).
   Objects on highly inclined orbits are associated with a maximum risk of collision because they can cross all the other orbits in their range of altitude. Such collisions can lead to very high mutual inclination - which in turn implies high impact velocities - due to the precessing orbital planes, caused by the Earth's oblateness. Compared to the above three factors, this one can be considered a "second-order" one.

Therefore, the definition of an index able to quantify and rank the criticality of an object abandoned in space, and the relevance of effects caused by its fragmentation on the long-term evolution of the space debris population,

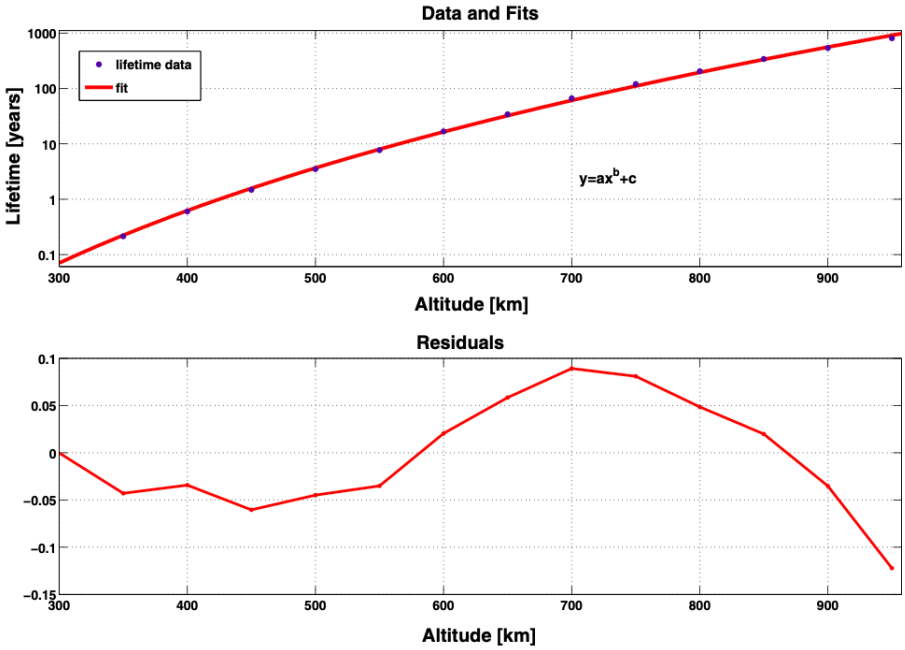

Figure 3.2: Orbital lifetime of a sample object with an area to mass ratio $A/M = 0.012 m^2 kg^{-1}$ as a function of altitude.

has to take into account these four main dependencies.
The CSI's final form as devised in [8] is:

$$\Xi = \frac{M(h)}{M_0}\frac{D(h)}{D_0}\frac{L(h)}{L(h_0)}\frac{1+c\Gamma(i)}{1+c}, \tag{3.2}$$

where $M_0, D_0, L(h_0)$ are properly defined normalizing factors for mass, spatial density and lifetime of the considered object: the reference mass M_0 is arbitrarily taken as 10,000 kg; the reference spatial density D_0 is the maximal spatial density of objects greater than 10 cm in size in the year 2009 (ρ_0 above) and it equals 6.8×10^{-8} $objects/km^3$. The $L(h_0)$ term is computed using eq. (3.1) and taking as reference value the corresponding lifetime at the altitude $h_0 = 1000$ km. $M(h), D(h), L(h)$ all depend on h, the orbital altitude of the object under consideration. Together with the object mass, h is the most influential parameter describing the environmental consequences of a given fragmentation. As for the last term, describing the inclination dependence, $\Gamma(i) = \frac{1-cos(i)}{2}$ and $c = 0.6$ since the typical flux of debris on an almost equatorial orbit is about 60% of the flux on a polar orbit. The Γ expression has been chosen instead of a simple $sin(i)$ term so as not to underweight the contribution of retrograde orbits. Using dimensionless quantities and a more compact form, the CSI associated with a given object becomes:

$$\Xi_k = m_k \rho_k L_k f_k(i), \tag{3.3}$$

where

$$f(i) = \frac{1+c\Gamma(i)}{1+c}. \tag{3.4}$$

3.2 The Shell Criticality (SC)

Even though the influence of orbital eccentricity upon the background object density as a function of orbital altitude (ρ) is taken into account, the CSI does not fully consider the effect of the target object eccentricity, which makes the object transit through different density regions. [9] first accounted for this effect, and proposed a more refined way to compute the CSI through the so-called **fractional CSI**: the LEO environment from 200 km to 2000 km of altitude is preliminarily subdivided in M spherical shells of thickness Δh[‡] Starting from ESA's MASTER 2009 population and employing again the SDM 4.2 suite, the average dimensionless density of objects ρ_j associated with each shell j is determined up to the epoch of concern, and the fractional contribution of an object k to the overall criticality of the altitude shell j is given by:

$$\Xi_{k,j} = \Phi_{k,j} m_k \rho_j L_k f_k(i) \tag{3.5}$$

where ρ_j is the dimensionless object density of the shell j and $\Phi_{k,j}$ is the fraction of orbital period that the object k spends inside the shell j. $\Phi_{k,j}$ can be computed from Kepler's equation and by means of geometrical considerations (see [9]) and its expression is:

$$\Phi_{k,j} = \begin{cases} 0 & r_{a,k} < R^j_{\text{in}} \text{ or } r_{p,k} > R^j_{\text{out}} \\ 1 & r_{p,k} > R^j_{\text{in}} \text{ and } r_{a,k} < R^j_{\text{out}} \\ \frac{E_{\text{out}} - E_{\text{in}} - e_k(\sin E_{\text{out}} - \sin E_{\text{in}})}{\pi} & r_{p,k} < R^j_{\text{in}} \text{ and } r_{a,k} > R^j_{\text{out}} \\ 1 - \frac{E_{\text{in}} - e_k \sin E_{\text{in}}}{\pi} & r_{p,k} < R^j_{\text{in}} \text{ and } R^j_{\text{in}} < r_{a,k} < R^j_{\text{out}} \\ \frac{E_{\text{out}} - e_k \sin E_{\text{out}}}{\pi} & R^j_{\text{in}} < r_{p,k} < R^j_{\text{out}} \text{ and } r_{a,k} > R^j_{\text{out}} \end{cases} \tag{3.6}$$

Having defined the fractional CSI, a more refined definition for the criticality of an object k can be derived, summing up all the contributions from each of the M shells making up the LEO environment:

$$\Xi_k = \sum_{j=1}^{M} \Xi_{k,j}. \tag{3.7}$$

This, in turn, allows to define: 1) the **shell criticality (SC)** of a given altitude shell j, as the sum of all individual criticalities of all N objects transiting through it:

$$\Xi_j = \sum_{k=1}^{N} \Xi_{k,j}, \tag{3.8}$$

and 2) the **overall criticality of the LEO environment**:

$$\Xi_{LEO} = \sum_{j=1}^{M} \Xi_j. \tag{3.9}$$

[‡]usually, $\Delta h = 50\ km$ offers a good discretization of the LEO region. In any case, the total number of shells (M) in which the LEO region is subdivided should be high enough (say, 30 or more) to avoid significant discretization errors.

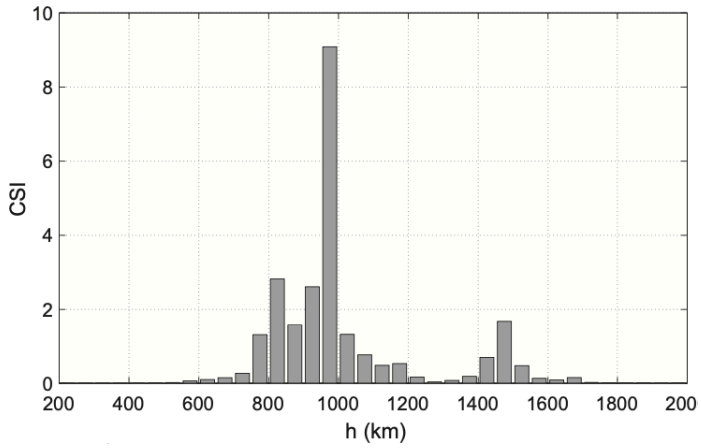

Figure 3.3: Overall criticality distribution as a function of altitude in the LEO region.

Figure 3.3 shows the overall criticality of the LEO region as a function of altitude. Comparing this figure with Fig. 3.1, it is interesting to note how the region between 950 and 1000 km of altitude is by far the most critical, while the crowded region at 750 km is associated with a lower overall LEO criticality, due to the presence of a residual atmospheric drag acting at lower h. For higher h, where the cleaning of the atmosphere is inefficient, the CSI basically reflects the spatial density of objects. This is clearly the case for the concentration around the altitude shell at $h = 1500$ km.

3.3 The Fragmentation Environmental Index (FEI)

The CSI and the SC indexes are both valuable tools that allow space agencies and other stakeholders to make informed decisions about future space activities. By assessing the risk associated with abandoned objects, it is possible to mitigate the risk of collisions and other hazards that could impact space exploration and other related activities. Nevertheless, neither of them is directly able to quantify and visualize the medium-term effects on the environment of an **in-orbit fragmentation**. The idea behind the FEI is exactly this: by quantifying the contribution of the fragments with respect to the original situation where the whole fragmented mass was contained in the intact object(s), one can obtain a first evaluation of the change in the environmental risk. As for the CSI, one such index must be quickly analytically calculable by means of a limited, through sufficient, number of parameters: it must be easily verifiable and repeatable. Guided by these principles, [1] attempted to highlight the effects of fragmentation on the environment considering the difference between the Ξ_{LEO} index (see eq. 3.9) before and after the event.

In general, a relevant in-orbit fragmentation is characterized by the creation of a large number of fragments. Since the 1970s, NASA has attempted to create a satellite breakup model to accurately predict the creation of a debris cloud following an explosion or collision. Such a model considers the size, area-to-mass ratio, and ejection velocity of each generated fragment, as these parameters are not constant for all debris. Distributions of the generated fragments as a function of a parameter such as mass or characteristic length (L_c, defined as the diameter of a spherical

particle equivalent to the irregularly generated fragment) are obtained by the model. The initial conditions of the breakup, such as collision velocity or the total mass of the parent object, have a significant impact on the event outcomes. In this context, a power law distribution has been developed based on laboratory hypervelocity impact experiments and from observations of fragments from in-space fragmentations (see [11]):

$$N(L_c) = 0.1M^{0.75}L_c^{-1.71}. \tag{3.10}$$

In the above equation, N is the number of expected fragments of a size equal to or greater than L_c (in meters). The value of M is defined as the sum of the masses (in kg) of both objects involved in a **catastrophic collision**[§]. In the case of a **non-catastrophic collision**, the value of M is defined as the mass (in kg) of the smaller object multiplied by the collision velocity (in km/s). In both cases, as shown for example in Fig 3.4, most of the fragments will be well below the current detection threshold of the European SST sensors (currently estimated (at best) around 15-20 cm in low-LEO (below $\approx$ 1000 km) and around 30 cm in high-LEO (between 1000 and 2000 km) [¶], meaning that any fragmentation event is expected to generate a plethora of non-trackable mm and cm-sized objects that will be not avoidable by active spacecraft. Given the average impact velocities in LEO (around 9-10 km/s) an impact against even these very small particles will lead to a very high kinetic energy and could be lethal for a medium size spacecraft causing the total loss of operations. Therefore it is important to estimate the contribution of this non-trackable portion of the generated debris cloud in each fragmentation, to readily compute the danger represented by a given event in the framework of a specific surveillance network with specific detection thresholds.

In order to properly take into account the hazard posed by different-sized objects, the CSI associated with a single object can be modified by introducing a **weighting factor** ω_{tr} in expression 3.2:

$$\Xi = \frac{M(h)}{M_0}\frac{D(h)}{D_0}\frac{L(h)}{L(h_0)}f(i)\omega_{tr}. \tag{3.11}$$

The weighting factor ω_{tr} satisfies $0 \leq \omega_{tr} \leq 1$, where $\omega_{tr} = 1$ for non-trackable objects, and it is dependent on the considered surveillance network. In a later section, we will discuss this dependence in more detail.
Moreover, following [12]), the cross-sectional area A of the objects can be included in the CSI definition, finally yielding:

$$\Xi = \frac{M(h)}{M_0}\frac{A}{A_0}\frac{D(h)}{D_0}\frac{L(h)}{L(h_0)}f(i)\omega_{tr}, \tag{3.12}$$

where the normalizing area is $A_0 = 1\,m^2$.
The weighted Ξ_{LEO} can be computed pre and post-fragmentation allowing to write the **Fragmentation Environmental Index** either in terms of absolute difference:

$$\Xi_{FEI} = \Xi_{LEO}(post) - \Xi_{LEO}(pre) \tag{3.13}$$

[§]A *catastrophic* impact is one in which both the target and the impactor are totally destroyed, producing a range of fragments. In a *non-catastrophic* impact the impactor is destroyed and the target is damaged (or cratered), but not totally destroyed.

[¶]Note that these are approximate values, derived by us from the main characteristics of the sensors typically used in the EU SST consortium and from the available literature. The actual values are not publicly disclosed.

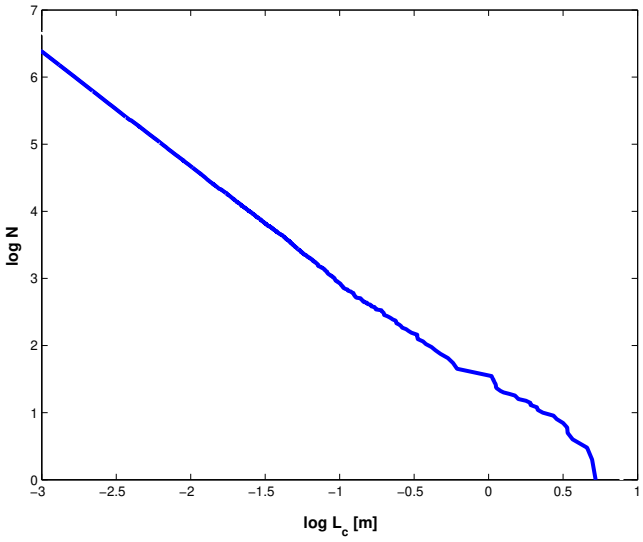

Figure 3.4: Cumulative distribution of the characteristic length L_c of the fragments generated in a collision between a 10 kg projectile impacting a 1000 kg spacecraft at 10 km/s, according to the NASA Breakup model.

or percentage difference:

$$\Xi_{FEI-PERC} = \frac{\Xi_{LEO}(post) - \Xi_{LEO}(pre)}{\Xi_{LEO}(pre)}. \tag{3.14}$$

As shown in [1], the FEI is capable of identifying areas in space that have been significantly disturbed due to fragmentation events, without relying on complex long-term population analysis (see Fig. 3.5). Its characteristics permit accurate predictions for short to medium time periods following the events.

By utilizing appropriate weighting factors, the index can efficiently identify specific debris populations that are of interest to any given sensor. In the following chapter, we propose new weighting factors with the aim of improving the FEI.

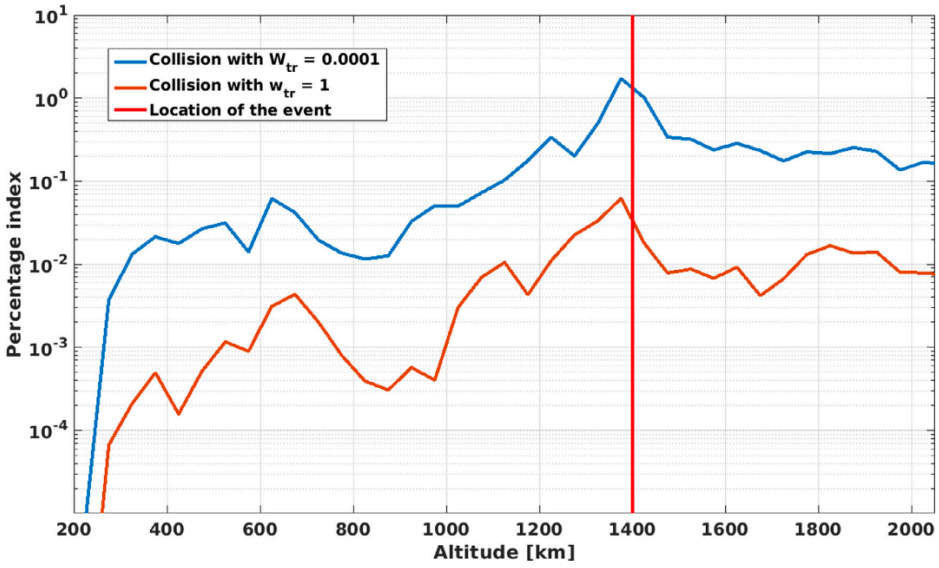

Figure 3.5: Percentage FEI for a collision between a 1000 kg satellite on a circular orbit at $\sim$ 1400 km of altitude against a 10 kg object, at 10 km/s, as computed 100 days after the event. Two cases corresponding to two different (constant) values of ω_{tr} are shown. The blue line (top one) shows the case with $\omega_{tr} = 0.0001$ while $\omega_{tr} = 1$ for the orange line. Credits: [1]

4

Improving the FEI

In the following, we will try to improve the FEI. As it can be understood, given the weighting factor introduced in Eq. 3.12, the index is strongly related to the considered sensor network, in particular to its sensitivity (e.g., expressed in terms of the size of the minimum detectable object). Therefore, we will first give a description of how a network of sensors is made, and what its components are. Then, we will try to give a generic definition of the FEI given the network and the considered fragmentation. Last but not least, we will try to apply these concepts to the specific case of the EUSST Network.

4.1 Generic Surveillance Network Description

A generic surveillance network of sensors must be able to detect, track, identify, and catalog space objects orbiting the Earth, whether they are space debris - such as inactive satellites and spent rocket bodies, or fragments coming from explosions or collisions. Sensors belonging to the network have to be distributed around the globe so as to give the best coverage of the whole sky. E.g., for the surveillance of the GEO ring, since the objects in that region appear "fixed" in the sky and do not transit in longitude, a distribution of telescopes along the whole Earth's longitude is required to monitor the complete GEO belt. On the other hand, for LEO surveys, the choice of longitude for the sensor location generally influences coverage less significantly than the choice of latitude. This can be explained by the Earth's rotation and by the observed uniform distribution of LEO orbits' longitude of the precessing ascending node. Hence, it is important to note that specific combinations of sensors, distributed over different areas, will be able to detect, track, and eventually catalog a different portion of orbital debris. Accurate planning is required in order to obtain the results that best fit one network's goals and a performance evaluation of the present and future network of sensors can only be made taking these factors into account.

4.1.1 Dedicated, Collateral and Contributing Sensors

Based on their assigned primary mission, the sensors of a network can be divided into three categories: dedicated, collateral, and contributing. **Dedicated** sensors have space surveillance support as their primary mission. **Collateral** sensors are those telescopes or radars whose primary mission is other than space surveillance support. These comprise military and aeronautical purpose radar systems, or sensors whose primary mission is to provide data about space launch vehicles. **Contributing** sensors provide space surveillance support upon request.

For the sake of this work, it will be worth recalling some basic properties of the sensors that make up a surveillance network - both optical and radar - as this information will be used for the determination of the network's overall capability, a parameter that will be considered in the FEI.

4.1.2 Optical Sensors

Optical sensors are strongly light-dependent, namely they gather light waves reflected off an object to form an image. In other words, their contribution during daylight or overcast sky conditions observations is null (new generation optical detectors that allow optical imaging of large LEO spacecraft even during daylight, close to twilight and sunset, are under study. Nonetheless, we can disregard these sensors for our current analysis). Two types of objects can be observed with an optical sensor: the ones that emit light and the ones that reflect it. In the case of orbital objects, photons from the Sun are reflected back or scattered by the target. Assuming the target object to be a simple plate of projected area A_t, its re-emitted power as received by the optical telescope is (at the entrance and neglecting the atmosphere):

$$P = A_t F_{\odot} \alpha_t \frac{A \cos \varepsilon_{t,in} \cos \varepsilon_{t,out}}{\rho_t^2} \tag{4.1}$$

where $F_{\odot}$ is the solar irradiance at 1 AU, and A is the collecting surface area of a telescope, A = $\pi D^2/4$, with D being the diameter of the telescope. The quantities $\varepsilon_{t,in}$, $\varepsilon_{t,out}$ represent the incident angles of the incoming and re-emitted photons. Note that P is inversely proportional to ρ_t^2, where ρ_t is the range from the telescope to the target. The relative brightness of an observed object is expressed in units of magnitude, according to:

$$mag = -2.5 \log_{10}(l/l_0) \tag{4.2}$$

where l is the object's brightness, and l_0 is the brightness of the star Vega, used as reference. The theoretical image resolution depends on the aperture diameter of the telescope, via the ratio D/λ, where λ is the wavelength of incoming light. However, the resolution limit of ground-based telescopes is limited to values less than 1" and is determined by local seeing conditions; moreover, the telescope's performance is constrained by the instrument efficiency and signal-to-noise (S/N) ratio. The smallest object size detectable by a Space Surveillance Network heavily depends on the telescopes and radars belonging to the network. As an example, the US Space Surveillance Network claims to be able to detect and track objects larger than about 10 cm in LEO and larger than about 1 m in GEO (refer, for instance, to Space-Track.org, the Space Situational Awareness Service by the U.S. Department of Defence). The performances of the European EUSST network are expected to be somehow lower due to the characteristics of its sensors.

4.1.3 Radar sensors

Radar sensors actively illuminate the target by means of energy beams coming from an antenna acting as a transmitter. The beam is then reflected off the target and returned to the receiver. Adverse meteorological conditions or the presence of a bright Moon jeopardize optical observations, but they don't affect radar observations, which are performed at frequencies within the radio window of the Earth's atmosphere. Radars can probe the sky continuously, as they can also observe during daytime. The power received P_r, is a function of the wavelength λ_e, the emitted power P_e, and the area of the emitter and the receiver antenna A_e and A_r . Moreover, it depends on the radar cross section A_{rcs}* and, of course, on the range to the target, ρ_t :

$$P_r = \frac{P_e A_e}{\lambda_e^2 \rho_t^2} \times \frac{A_{rcs}}{4\pi\rho_t^2} \times A_r \tag{4.4}$$

Therefore, the received power of a radar echo increases with increasing antenna aperture (both of the receiver and emitter) and emitting power, and it decreases both as the wavelength of the radar increases, and as the target distance increases. In particular, it is inversely proportional to ρ_t^4. Primarily due to this last caveat, radars are mostly used to detect and track objects at low LEO altitudes, while optical sensors are employed to observe objects in higher orbital regions (i.e., higher LEO, MEO and GEO).

Radar sensors can be roughly divided into two types: **mechanical radars** and **phased-array radars.** The former can follow the target throughout its coverage, but it can only track one object at a time. They can be *monostatic* radars if the transmit antenna coincides with the receive one, or *bistatic*, if the two are separated. On the other hand, phased-array radars are many thousands of small transmit/receive antennas placed on the side or face of a large wedge-shaped structure. This allows for multiple beams to be sent at the same time, namely a phased array radar is capable of tracking multiple targets at the same time. These new technology radars have a high cost of building and maintenance.

Both reflector antennas and phased arrays can measure the time it takes for the signal to be transmitted and received back upon reflection from the target. Labelling with t_r the reception time and with t_t the transmission time, the two-way signal is given by:

$$\Delta t_{2w} = t_r - t_t \tag{4.5}$$

Radars also allow to get information on the target position and observer-target relative velocity. Indeed, the range can be expressed as:

$$\rho \sim \frac{1}{2} c \Delta t_{2w} \tag{4.6}$$

with c being the speed of light in the vacuum. On the other hand, the signal, transmitted at a known specific frequency f_t, will be characterized by a different receiving frequency, f_r. The corresponding Doppler shift, Δf_{2w}

*The radar cross section (RCS) depends on the target's material, shape, and orientation, as well as on the ratio of a characteristic object dimension to the radar wavelength, l_t/λ . It is expressed in decibel square meters and it is a radar equivalent of the visual magnitude in optical observations:

$$A_{rcs}[dBsm] = 10 log_{10}(A_{rcs}/[m^2]) \tag{4.3}$$

can be used to determine the range-rate $\dot{\rho}$:

$$\dot{\rho} \sim -c\frac{\Delta f_{2w}}{f_t} \tag{4.7}$$

More accurate expression must account for relativistic and refraction corrections on the path of the radar signal. Other important quantities that can be inferred by means of radar measurements are the azimuth and elevation angles, A and h of the maximum gain pointing direction, the received power P, and the polarization change in the radar pulse. The latter can help reveal the structure, orientation, and environmental conditions of the surface elements.

4.2 Space Debris Detection and Tracking

Upon detection of space debris, tracking is of paramount importance for any Surveillance Network, as it allows for precise orbit determination and cataloguing of the observed objects. As it is well known (see, for instance: [13]), the knowledge of **at least** 4 of the 6 orbital elements characterizing a satellite's orbit are needed to be able to predict subsequent passes at a later time, and therefore to plan follow up observations of the target. In other words, 2 or more observations of the target taken at different times are needed to get **preliminary** orbit determination. The Initial Orbit (**IO**) thus obtained, **assumed to be circular**, can be used to plan future observations to retrieve the full set of six orbital elements. Then, to accurately propagate an orbit into the future from a set of initial observations requires taking the various perturbations, as well as instrumentation errors themselves, into account. It is clear that a Surveillance Network characterized by both dedicated survey and tracking sensors will be considered more efficient than the extreme case of a network made of sensors of just one type. The two main sensor modes - survey and tracking mode - are described in the following, both in the case of optical and radar sensors.

4.2.1 Surveying

Optical Surveys: Inertially Staring Mode

All objects in Near-Earth orbits as seen by optical telescopes on Earth appear as fast-moving objects with angular velocities that can range from a few arcsec/second to more than 1,000 arcsec/second with respect to the stellar background. The magnitude of a debris object depends on its illumination, distance, size, and light reflection properties at the observation epoch, and many of them are faint. The requirements for the optical sensors to be used in these surveys are very similar to the corresponding demands for systems used in surveys for minor planets and near-Earth objects. More specifically, a good survey telescope is characterized by **fast optics** and very **large field of view**.

In the **inertially staring mode**, also called "sidereal tracking" an optical sensor follows the apparent motion of the stars, keeping them always in the same field of view. The resulting image is characterized by the presence of both stars and moving objects. The former is fixed and can be erased using image processing algorithms, while the latter will appear as tiny streaks (see Fig. 4.1). Precise timing mechanisms are needed, as the observation epochs need to be very accurate, and the relative position of a streak with respect to the stars (whose coordinates are well-known)

can be retrieved by means of astrometric software, in order to calculate the position of the moving object. This information is then used either to identify a new object (a so-called "uncorrelated" target) or to update the already existing catalogue of orbiting objects. Efficient strategies of optical surveys have been studied in detail for the GEO and MEO regimes (see, for example, [14] and [15]) while only recently [16] have tried to address the problem of surveys in terms of statistical coverage in the LEO region.

Figure 4.1: A satellite streak amongst a field of stars acquired in staring mode. Credits: John McGraw, "Angles and Range: Initial Orbital Determination with the Air Force Space Surveillance Telescope (AFSST)"

Radar Surveys: Beam Park Mode

In beam-park mode, a radar beam is kept in a fixed direction with respect to the Earth, while objects passing through the beam are tracked. In 24 hours, as a result of the Earth's rotation, the radar effectively scans a narrow strip through 4π steradians of the celestial sphere. Both mechanical and phased array radars can be operated in beam park mode. The beam-park mode can be used to detect both previously known and uncatalogued objects at any altitude, provided that the reflected power captured by the receiver can be distinguished from the noise. Operating sensors in this way is a useful way mainly to estimate statistical coverage of the debris environment.
In 1991, the American Target Resolution and Discrimination Experiment (TRADEX) was one of the first dedicated radar systems exploiting the beam park mode for space surveillance purposes (see Fig. 4.2a). It was able to detect a total of 19 objects with an estimated size of 3-4 cm over the course of a 4.4-hour campaign, probing itself to be a powerful tool. As concerning European countries, the European Incoherent Scientific Association

(EISCAT) system has been one of the primary sources of radar measurements related to space debris. The EISCAT Svalbard Radar (ESR) located in Longyearbyen, in the Svalbard islands (see Fig. 4.2b), was employed for a two-year campaign from March 2007 to March 2008, in an attempt to extend the previous dedicated 2000 hours of observations to continuous coverage. This resulted in the detection of 23.900 events in beam park mode, with the smallest detected object in the range 700 - 1000 km of altitude being 3.5 cm in size.

(a) The TRADEX radar antenna.

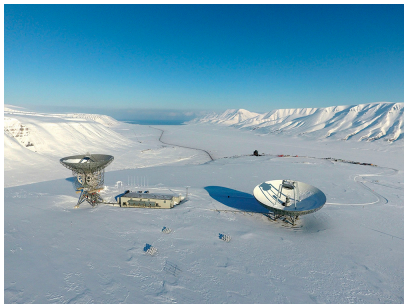

(b) The ESR radar system.

4.2.2 Tracking

Optical Tracking Mode

If the telescope is in tracking mode an observed object is kept in the field of view by moving the sensor following the apparent motion of the object in the sky. Then the moving object is seen as a point source on a background of streaks caused by the stars. E.g., an optical telescope tracking a fragmentation event in LEO must be able to follow the objects while they trace a given arc along their orbit. This typically requires fast slew rates in LEO, as most objects in that region move at a speed between 200 and 700 arcsec/sec ([16]).

Radar Tracking Mode

Tracking an object requires preliminary knowledge of the object's position in order for the radar to know where to point at to start chasing it. Within Europe, one of the most prominent examples of such radars implementing tracking mode is the Grand Réseau Adapté a la Veille Spatiale (GRAVES). The GRAVES is a bistatic radar, with its transmitter located near Dijon (France) and its receiver 400 km further south, in Provence. The transmitting unit consists of 4 antenna patch arrays, while the receiving segment is a 60 m diameter sparse array. Another unique example is given by the Tracking and Imaging Radar located in Watchberg, Germany. As the name suggests, the TIRA system comprises a tracking radar and an imaging radar. The radome accommodates an antenna with a diameter of 34 meters. The movable part weighs 240 tons and can be turned at a speed of 24° per second. A full rotation takes 15 seconds.

4.3 Network's Detection Performance

This subsection is dedicated to the estimation of the capabilities of both passive and active networks of sensors, when it comes to an in-orbit fragmentation. Defining an optical and radar detection performance in terms of the sensor's characteristics is important to be able to define new weighting factors that will enter the *FEI*. This can be done by writing down a "**Detectability Function**" that takes into account the observables and the conditions to detect an object, given the sensor specifics.

4.3.1 Optical Detection Performance

To start off, we turn to the **passive** set of sensors and we try to specialize (4.2) to a given fragment. Some new optical instruments, having large Field Of Views (typically larger than 5° per aperture) and conceived with the objective of characterizing transient events like planetary transits or gamma-ray bursts (see, for instance: [17], [18], [19]) have proven to be particularly suited for high-volume monitoring of orbital debris. Ongoing research, such as [2] aims at optimizing these sensors' integration times, and builds upon this idea in order to determine such a telescope's network detection performance in various orbital regimes.

For our purposes, we can make the simplifying assumption of approximating every fragment to a sphere. In this case, it may be shown that the object's magnitude in the **visual band** is given by:

$$m_{obj} = m_{sun} - 2.5 \log \left(\frac{s^2}{\rho^2} r p(\Upsilon) \right) \tag{4.8}$$

where s is the diameter (size) of the object, ρ is the range to the object from the observer, r is its reflectance, and $p(\Upsilon)$ is the solar phase angle function, meaning the angle between the observer and the sun, relative to the fragment. Speaking of r, we will assume for our estimates equal contributions from both specular and diffuse reflectance components of r (this is supported by observational data), and we will consider a gray body reflectance for all objects, such that r is constant at all wavelengths. The estimated debris optical albedo r has been recently revised, with recent work by [20] establishing a mean value of $r = 0.175$ for fragmented space debris. The function $p(\Upsilon)$ is divided in specular phase angle function, $p_{spec}(\Upsilon)$ and diffuse phase angle function, $p_{diff}(\Upsilon)$. The former is constant, and its value is $1/4$, while the latter is given by ([2]):

$$p_{diff}(\Upsilon) = \frac{2}{3\pi} [sin(\Upsilon) + (\pi - \Upsilon) cos(\Upsilon)] \tag{4.9}$$

For simplicity, we will always assume Υ to be equal to 90, so that

$$p_{diff}(\Upsilon) = \frac{2}{3\pi} \tag{4.10}$$

is constant. (4.8) then may be rewritten as:

$$m_{obj} = m_{sun} - 2.5 \log \left[\frac{s^2}{\rho^2} \frac{2}{3\pi} r \right] \tag{4.11}$$

However, visual magnitudes alone do not allow for a physics-based assessment of sensor performance. Absolute radiometric units, such as **irradiance** in terms of photon flux (photons/second/area) is required to evaluate passive sensing performance. The conversion is given by (see again [2]):

$$E_{RSO} = 5.6 \times 10^{10} \cdot 10^{-0.4 m_{obj}} \tag{4.12}$$

and it is measured in $ph/s/m^2$. In the equation above, *RSO* stands for "Resident Space Object". For reference, 20 cm targets at a range of 2000 km are associated with an apparent magnitude of about 12.8 m_v, or irradiance of $\sim 4.2 \times 10^5$ $ph/s/m^2$, as computed by software that has been developed for this work. Furthermore, the performance of an optical sensor depends on the **angular velocity** of an object relative to the ground. When viewed at high elevation angles, lower altitude LEO objects may exceed **angular rates** of one degree per second, corresponding to 3600 arcsec/s. Telescopes pointing at lower elevation angles are therefore preferred. Moreover, it is known that the volume of observable objects dramatically increases with decreasing elevation angles. The drawback, though, is that the range to a specific object increases with decreasing elevation angle, and so does its apparent magnitude. For instance, objects orbiting in an 800 km altitude orbit are associated with a range of around 1400 km if seen from a ground-based sensor elevated at a 30° angle. [2] plots a range of LEO RSO angular velocities as seen from the ground, function of the elevation angle, for different circular orbit altitudes - see 4.3. It can be checked that most objects at 300 km altitudes (low LEO) are seen as fast-moving objects: if we assume an

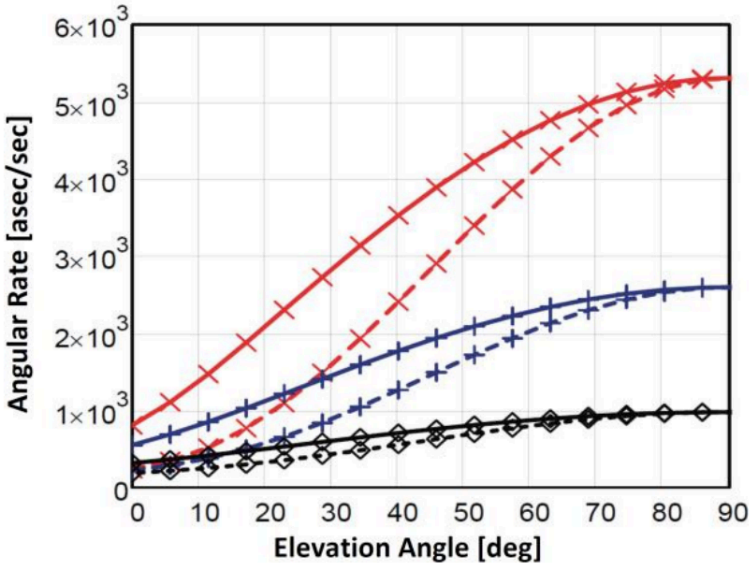

Figure 4.3: LEO RSO typical angular rates (in arcsec/sec) as seen from the ground, as a function of the telescope's elevation angle. Black, Blue and Red lines represent respectively circular orbits with 300 km, 600 km and 1500 km altitudes. The solid lines represent the maximum angular rate, the dotted lines the minimum. Credits: [2]

elevation of 30°, the corresponding angular speed ranges between 2000 *arcsec/sec* and 3000 *arcsec/sec*. At 600 km, the average angular rate goes down and it is seen to take values in the interval 1000 *arcsec/sec* and 2000 *arcsec/sec*. The slowest fragments are of course the ones populating the high LEO region: already at around 1500 km, their speed is always below 1000 *arcsec/sec*. Note that other factors influence the typical pointing directions of a given telescope, depending also on the minimum permitted elevation related to atmospheric disturbances and sensor specifics (e.g., limiting the range of the mounting system).

Angular rates (ARs) and irradiance (E_{RSO}) are important quantities when it comes to space objects detection, because they enter the **Signal to Noise Ratio (SNR)** equation. Indeed, detecting a fragment is accomplished by applying a threshold to the counts for each pixel while accounting for known objects and noise contributions. In other words, to detect an object means to look for signals of interest in the noise pattern. In our case, the signal-to-noise ratio provided in terms of photoelectrons **per pixel** is given by:

$$SNR_{optical} = \frac{e_s}{\sqrt{e_b^2 + e_n^2 + e_{shot}}} \tag{4.13}$$

† where e_s is the number of signal photoelectrons:

$$e_s = QE \cdot \tau \cdot A \cdot \tau_{atm} \cdot E_{RSO} \cdot t_{sig} \tag{4.14}$$

†Please note that we are neglecting dark noise and other noise sources as they are negligible for modern detectors with the integration times of interest.

e_b is the number of background photoelectrons:

$$e_b = QE \cdot \tau \cdot L_b \cdot A \cdot \tau_{atm} \cdot \mu^2 \cdot t \tag{4.15}$$

and e_n is read noise from the detector in terms of photoelectrons, and e_{shot} is the detection-event-associated shot noise. Shot noise represents the statistical variation of a source's photon emissions over time, and it can be modeled by a Poisson process. We may rewrite (4.13) as:

$$SNR_{optical} = \frac{QE \cdot \tau \cdot A \cdot \tau_{atm} \cdot E_{RSO} \cdot t_{sig}}{\sqrt{QE \cdot \tau \cdot L_b \cdot A \cdot \tau_{atm} \cdot \mu^2 \cdot t + e_n^2 + e_{shot}}} \tag{4.16}$$

In the above equations, QE is the so-called quantum efficiency of the detector, τ and τ_{atm} are the optical and atmospheric transmittance, both responsible of some signal loss, $A = \pi d^2/4$, t_{sig} is the ***signal*** integration time (per pixel) of interest, which generally differs from the ***system*** integration time t, due to the angular movement of the object during an exposure period. The maximum signal possible is obtained when the fragment moves through the full length of a pixel during an exposure. L_b is the conversion from background signal magnitude to radiometric units:

$$L_b = 5.6 \times 10^{10} \cdot 10^{-0.4 m_{background}} \cdot \left(\frac{180}{\pi}\right)^2 \cdot 3600^2 \tag{4.17}$$

where $m_{background}$ is the surface brightness associated with the background in units of $mag/arcsec^2$. Finally, $\mu = x/f$ is a sensor-related quantity, given by the individual detector size, x, divided by the focal length, f. Recording a detection event thus translates into choosing a suitable threshold for the SNR above which a Resident Space Object can be detected with a low false alarm rate. As noted in [2], an SNR of six already provides good detection performance. [‡] More in general, high SNR thresholds such as the ones required for fragments detection, allow us to reasonably assume a **background-dominated case**, for which $e_b >> e_s, e_n$. Under this assumptions, 4.16 becomes:

$$SNR_{optical} = \frac{QE \cdot \tau \cdot A \cdot \tau_{atm} \cdot E_{RSO} \cdot t_{sig}}{\sqrt{QE \cdot \tau \cdot L_b \cdot A \cdot \tau_{atm} \cdot \mu^2 \cdot t}} \tag{4.18}$$

It is therefore clear that, given a specific sensor with its associated QE, μ, A, t and τ, together with an estimation of the typical τ_{atm} , and considering the suitable case where the background radiance L_b dominates the detector read noise, the $SNR_{optical}$ equation will only depend on the quantities E_{RSO} and t_{sig}:

$$SNR_{optical} \propto E_{RSO} \times \frac{t_{sig}}{\sqrt{t}} \tag{4.19}$$

In turn, E_{RSO} ultimately depends on the size of the fragment and the range to the target: $E_{RSO}(s, \rho)$. Assuming a fixed 30° elevation angle for all telescopes and circular orbits for the targets, it is possible to relate ρ measurements to corresponding LEO altitudes h. Indeed, from the *slant range* equation and solving for h, one gets:

[‡]An SNR value greater or equal to six is also used in the orbit propagation and observation simulations approach as described in [21], where the efficiency of a network of the new Flyeye telescopes in carrying out HLEO region surveys is addressed.

$$h = \sqrt{r_E^2 + \rho^2 - 2r_{\oplus}\rho\cos(90 + \varepsilon_0)} \tag{4.20}$$

ε_0 being the elevation angle, $r_{\oplus}$ being the Earth's radius and ρ the target's slant range. Then we can write $E_{RSO} = E_{RSO}(s, h)$.
On the other hand, t_{sig} can be estimated (as an order of magnitude) to be

$$t_{sig} = \frac{\mu}{AR}, \tag{4.21}$$

where AR is the object angular rate with respect to the telescope pointing. Note that this is also the maximum time equal to the transit time through a single pixel on the detector with angular extent μ. If we could take $t = t_{sig}$, we would optimize the $SNR_{optical}$, and have the simpler equation:

$$SNR_{optical} = \sqrt{QE \cdot \tau \cdot A}\frac{\tau_{atm} \cdot E_{RSO}}{\sqrt{L_b \cdot AR \cdot \mu}} \tag{4.22}$$

However, this can't be done practically, because it would require *a priori* knowledge of the debris angular rate, and, in most cases, the object transits more than just one pixel during an exposure. A more realistic estimate is obtained by degrading the optimal $SNR_{optical}$ equation by a factor of $\sqrt{2}$. (see [2]):

$$SNR_{optical} = \frac{1}{\sqrt{2}}\sqrt{QE \cdot \tau \cdot A}\frac{\tau_{atm} \cdot E_{RSO}}{\sqrt{L_b \cdot AR \cdot \mu}} \tag{4.23}$$

Optical Observability Function

As we have discussed above, we can argue that the angular rate of an object roughly depends on its altitude (low LEO, medium LEO, high LEO). This tells us that t_{sig} depends on h, $t_{sig} = t_{sig}(h)$, because ultimately $AR = AR(h)$.

Therefore, for the sake of this work, we define a function of the two parameters ***size*** and ***altitude***, $\mathcal{F}(s, h)$:

$$\mathcal{F}(s, h) = A\omega_{E_{RSO}}(s, h) + \omega_{AR}(h) \tag{4.24}$$

that is a **linear combination** of two separate weights: one describing the capability of a telescope to detect faint objects, and the other related to how fast the object transits in a given field of view. In the above equation, **A is a network-related coefficient**.
More specifically, if we subdivide the LEO environment as in table 4.3.1, then, referring to the plot in 4.3, we can tailor the function $\mathcal{F}(s, h)$ to our network capabilities (i.e. we can assign A a specific value).

Altitude h	**Region**
0 < h < 500 km	low LEO
500 < h < 1000	medium LEO
1000 < h < 2000	high LEO

For instance, let's assume the ideal case in which the debris cloud is very slow, in terms of angular rate in the sky. This would lead to a function $\mathcal{F}(s, h)$ depends only on the observed irradiance of the given fragment, the value of $AR(h)$ not affecting performance (all telescopes are assumed to be able to observe a very slow-moving cloud). However, this situation wouldn't be representative of reality. Therefore, we assume that only a few percentage of telescopes is going to be able to observe the fastest fragmentations - i.e. those happening in low-LEO. A realistic network could be characterized by the following: 10% of the network is able to follow fragments moving at angular rates greater or equal than 2000 *arcsec/sec*; 50% of the network is able to follow fragments with angular rates between 1000 and 2000 *arcsec/sec*, and 100% of the network is able to follow fragments with angular rates lower than 1000 *arcsec/sec* (this is also justified by the fact that, according to [16], most telescopes are able to detect objects moving at $\sim$ 1800 arcsec/sec). In other words, the real situation is well described by an exchange between how good the observations are in terms of 1) object's magnitude - how bright the object appears - and 2) the object's angular rate - how fast it moves relatively to the observer - and the two weights in (4.24) are intertwined. In this framework, the coefficient A gives us a feeling of the relative importance of the $\omega_{E_{RSO}}$ and ω_{AR} contributions. For a fragmentation happening in low LEO, we set $A = 0.1$, meaning that we give more importance to the latter. This is because we expect a fragment belonging to such a cloud to be the "brightest it can be", but also the "fastest it can be". Applying this reasoning to the other two orbital regimes, we set $A = 0.5$ if the cloud is found in medium LEO, and $A = 1$ for a debris cloud in high LEO. This latter condition also amounts to shutting down the $\omega_{AR}(h)$ contribute for a fragmentation happening in high LEO (see next paragraph). Resuming what we just said, the A coefficient will depend on where in the LEO region the fragmentation has happened, and its value for the three different regimes is given in table 4.1.

REGION	LOW LEO	MEDIUM LEO	HIGH LEO
A	0.1	0.5	1

Table 4.1: Value of the A coefficient as it appears in the function $\mathcal{F}(s, h)$.

A New Optical Weight

So far, we have defined the function $\mathcal{F}$, but we never made explicit the forms of the two weights entering the equation. Here we describe a way to establish them.

We start from the assumption of having a number $N_{optical}$ of telescopes, all sharing the same characteristics: every optical sensor can probe the LEO environment up to an altitude h_{max}, say $h_{max} = 2000\ km$ of altitude, and is able to detect all fragments greater than $s_{min} = 20\ cm$ in size.[§]. Assuming all telescopes to have a 30° elevation, the range corresponding to a 2000 *km* altitude shell is given by the slant range equation (4.20) and it amounts to $\rho_{max} \sim 3110$ km. The corresponding limit magnitude is given by (4.8), with $s = 20\ cm$ and $\rho = 3110\ km$. This yields $m_{20,2000} \sim 12.56\ m_v$. This magnitude corresponds to what we can call the "**detectability limit**" of our network. In the case where we have access to a generic knowledge of the target's range - for instance, given by

[§]While this is a useful assumption, it's crucial to emphasize that, as of the present moment, radar sensors exclusively handle tracking below altitudes of 1000 *km*. The future envisions the utilization of telescopes for surveillance and tracking purposes in low Earth orbit (LEO), but presently, they are primarily utilized for observations in MEO and GEO.

the first estimates of the orbit coming from the largest observed fragments - we can use (4.20) to get the target's altitude, and every fragment smaller than 20 *cm* at the fragmentation altitude h_{frag} has to satisfy:

$$m_{s_{frag},h_{frag}} \leq m_{20,2000} \tag{4.25}$$

where s_{frag} is the fragment size, in order to be detected. Therefore, the first thing to check is for this condition to hold for a given fragment: we won't be able to detect it otherwise. It is important to note that, since the limiting magnitude of a telescope can be approximated by the formula (see [22] for more):

$$m_{lim} = 5\log(D_{lim}) + 7.69, \tag{4.26}$$

condition 4.25 sets the diameter **(in centimetres)** of an average telescope describing our network. In the specific case where $s_{min} = 20\ cm$ and $h_{max} = 2000\ km$:

$$m_{lim} = m_{20,2000} = 12.8 m_v \implies D_{lim} \sim 10cm \tag{4.27}$$

In practical terms, when we establish a detectability limit for the network, we are essentially describing it as a telescope with a diameter D_{lim}.
Keeping this in mind, consider only the fragments we are able to observe and define the weight:

$$\omega_{E_{RSO}} = 1 - \frac{E_{RSO}(s_{frag}, h_{frag})}{E_{RSO}(s_{min}, h_{frag})} \tag{4.28}$$

where $s_{min} = 20\ cm$ and h_{frag} is the altitude of the fragment, assuming it to be on a **circular orbit**.[¶] Please note the choice of h_{frag} at the denominator. This is needed if we want to have an always-positive weight belonging to the interval $[0, 1]$. Indeed, had we chosen h_{max} in place of h_{frag}, we would have found that observed fragments smaller than s_{min}, at an altitude lower than h_{max}, would be characterized by an E_{RSO} signal *greater* than $E_{s_{min},h_{max}}$, therefore producing ***negative*** weights. We associate the fragments for which condition (4.25) does not hold with maximum risk, while we give a null weight to fragments bigger or equal to 20 *cm* in size:

$$\begin{cases} \omega_{E_{RSO}} = 1 - \frac{E_{RSO}(s_{frag},h_{frag})}{E_{RSO}(s_{min},h_{frag})}, & \text{if } m_{s_{frag},h_{frag}} \leq m_{20,2000} \\ \omega_{E_{RSO}} = 1, & \text{if } m_{s_{frag},h_{frag}} > m_{20,2000} \\ \omega_{E_{RSO}} = 0, & \text{if } s_{frag} \geq 20cm \end{cases}$$

By doing this, we have assigned a weight to the E_{RSO} contribution to the $\mathcal{F}(s, h)$ function, namely $\omega_{E_{RSO}}(s, h)$. As for $\omega_{AR}(h)$, we make use of the LEO subdivision mentioned above and 4.3 and define:

- $AR_{HLEO} \sim 500$ arcsec/sec;
- $AR_{MLEO} \sim 1000$ arcsec/sec;
- $AR_{LLEO} \sim 2000$ arcsec/sec.

[¶] In other words, given the semi-major axis a_{frag}, $h_{frag} = a_{frag} - r_{\oplus}$, with $r_{\oplus} = 6378$ km being the Earth's radius.

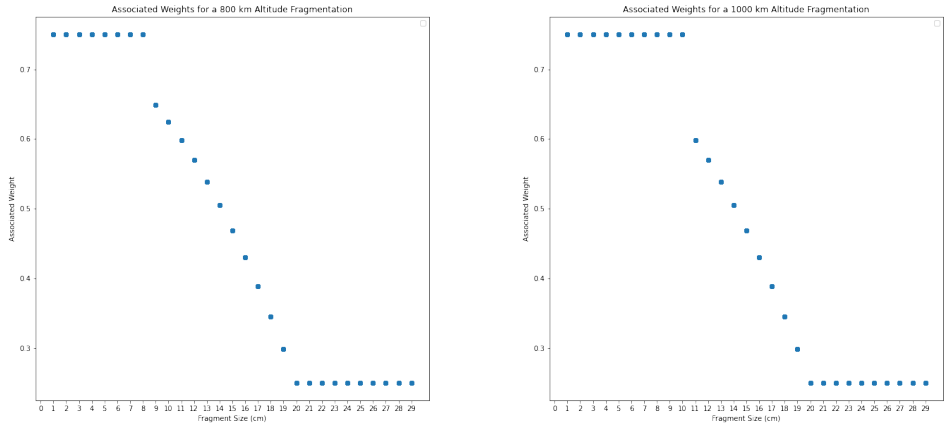

(a) Associated $\mathcal{F}$ weight for fragments up to 30 cm in an 800 km altitude orbit.

(b) Associated $\mathcal{F}$ weight for fragments up to 30 cm in a 1000 km altitude orbit.

Figure 4.4: Simulated $\mathcal{F}$ weights for two different fragmentation cases.

The separation into three regions allows us to define the following weight:

$$\begin{cases} \omega_{AR} = 1 - \frac{AR_{HLEO}}{AR_{LLEO}}, & \text{if fragment in low LEO} \\ \omega_{AR} = 1 - \frac{AR_{HLEO}}{AR_{MLEO}}, & \text{if fragment in medium LEO} \\ \omega_{AR} = 0, & \text{if fragment in high LEO} \end{cases}$$

We wrote a Python script that, given the telescope's elevation and diameter, computes the risk associated with **simulated** random fragments of various sizes (values of the $\mathcal{F}$ function). ‖ Figure 4.4 shows the results for a fragmentation happening in an 800 km and 1000 km altitude shell, respectively. For each plot, there are two size regions for which the associated weight takes either maximum or minimum values.

The former represents the non-visible fragments, i.e. those fragments for which $\omega_{E_{RSO}} = 1$, because they don't satisfy (4.25); the latter is characterized by those fragments greater or equal to s_{min} in size.
In between, there's a whole range of sizes for which $\mathcal{F}(s, h)$ takes values in the interval $[\omega_{min}, \omega_{max}]$. These are seen to be well-fitted by a second-order polynomial, see Figure 4.5.

A first-order fit showcases generally **larger residuals**; nevertheless, it might be insightful to display it on the same chart, as a straight line can also be approximated by the simple parametrization:

$$\frac{y - y_1}{x - x_1} = \frac{y_2 - y_1}{x_2 - x_1} \tag{4.29}$$

‖Unlike the results we will show later in section 5, the current fragments **are not** representative of an actual cloud, in the sense that they do not follow a specific mass distribution. We rather generated some sizes in the interval $0 - 20$ cm and plotted the results to have a better grasp on the different weights associated with different fragments.

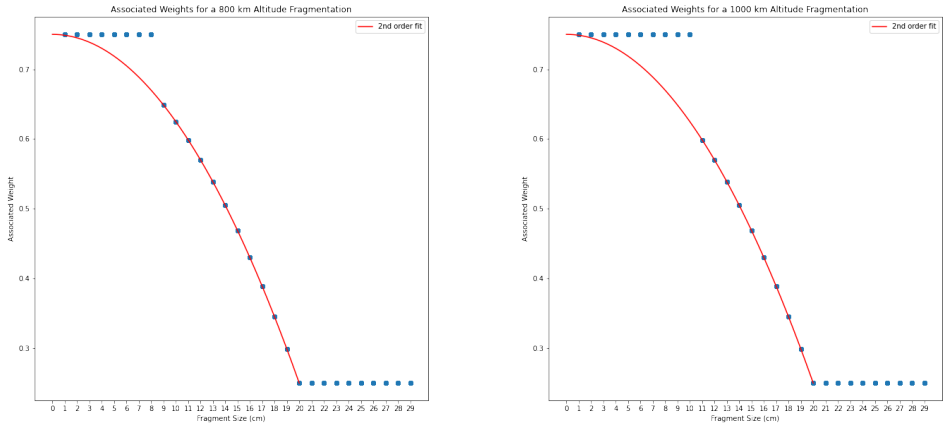

(a) Associated $\mathcal{F}$ weight for fragments up to 30 cm in an 800 km altitude orbit.

(b) Associated $\mathcal{F}$ weight for fragments up to 30 cm in a 1000 km altitude orbit.

Figure 4.5: Simulated $\mathcal{F}$ weights for two different fragmentation cases. The middle part of the plot is well-fitted by a second-order polynomial (red line).

which is the equation of a line passing by two given points, them being: $\left(x_1, y_1\right) = \left(\mathcal{F}(s_{threshold}, h_{frag}), s_{threshold}\right)$, with $s_{threshold}$ the size of the smallest detectable fragment capable of producing the lowest detectable signal at the fragmentation altitude h_{frag}, and $\left(x_2, y_2\right) = \left(\mathcal{F}(s_{min}, h_{frag}), s_{min}\right)$. While acknowledging the limitations of linear parametrization, it may serve as a tool to provide the operator with a preliminary estimate of the weight associated with a specific fragment, considering the telescope's characteristics, as illustrated in Fig. 4.6.

In other words, given the optical network specifics and the altitude of the fragmentation (both known), we are able to associate each fragment size with a different value of the **optical weight**, by means of a simple linear parametrization that takes into account only the minimum detectable fragment at that specific altitude h_{frag}, and the minimum detectable fragment at the maximum altitude h_{max}.

As we will see in the next sections, given an in-orbit fragmentation, it is straightforward to compute the overall risk associated with the debris cloud by summing up the single fragments' contributions to the **fractional CSI**.

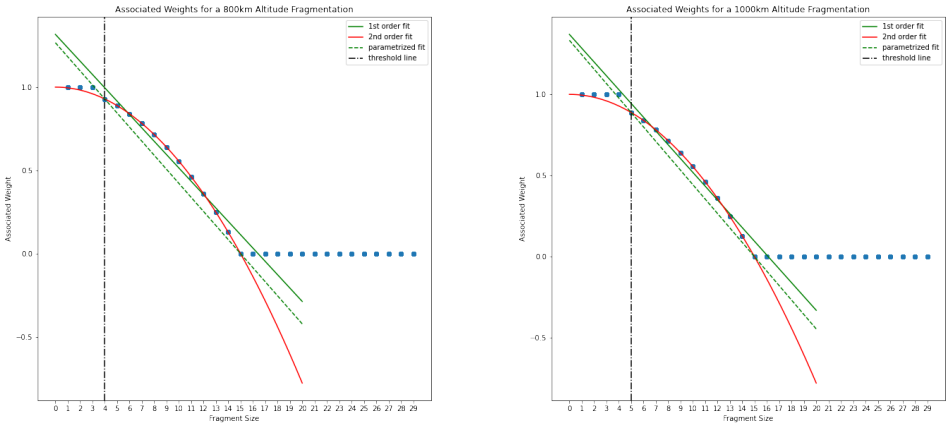

(a) Associated $\mathcal{F}$ weight for fragments up to 30 cm in an 800 km altitude orbit.

(b) Associated $\mathcal{F}$ weight for fragments up to 30 cm in a 1000 km altitude orbit.

Figure 4.6: Simulated $\mathcal{F}$ weights for two different fragmentation cases. The middle part of the plot is well-fitted by a second-order polynomial red line). A first-order fit (green solid line) and the parametrized fit (green dotted line) performed as described above are also displayed.

4.3.2 Radar Detection Performance

Radar detection of space debris is usually done either via beam park experiments (mainly for space debris environmental studies) or, typically at a lower level of sensitivity, by continuous surveys from the SST sensors. As already done for telescopes, we can describe the radar performance by the following form of the radar range equation, where the ratio between P_S, the signal in the radar receiver, and P_N, the noise signal is considered:

$$SNR_{radar} = P_S/P_N = \frac{P_T G_T G_R \lambda^2}{(4\pi)^3 k T_0 B F_n L} \frac{\sigma}{\rho^4} \tag{4.30}$$

The interesting dependencies in equation (4.30) are the ones on the far right, namely the ρ^{-4} and σ terms, where ρ is the object's range and σ is the *radar cross section* **(RCS)**. All other appearing terms constitute the *design parameters*, and they depend on the specific radar sensors. Here we list them:

- P_T, the *peak transmit power* specified at the output of the transmitter, measured in Watts (W);
- G_T and G_R , transmit and receive antenna transmitting gains. They're both dimensionless;
- λ, the operating radar wavelength in meters (m)
- k, Boltzmann constant, equal to 1.380×10^{-23} $\frac{W}{Hz \cdot K}$
- T_0 , a reference temperature in Kelvin (K), usually set to $T_0 = 290\ K$
- B, the ***effective*** noise bandwidth of the radar. It is measured in Hertz (Hz).
- F_n , the radar noise figure. It is dimensionless.

- L, a factor that takes into account losses that need to be considered when using the radar range equation, such as the antenna and feed losses.

The following explanation gives a feeling of why ρ enters the equation with a power of -4 in the case of a monostatic radar.
Let P_T be the transmitted power, G the antenna gain, and ρ the distance of the target. The power density at the target is:

$$P_D = \frac{P_T G_T}{4\pi\rho^2} \tag{4.31}$$

If we assume an isotropically radiating target of cross-section σ, the P_D portion transmitted back to the radar is:

$$P_D^{'} = \frac{P_D \sigma}{4\pi\rho^2} = \frac{P_T G_T \sigma}{(4\pi\rho^2)^2} \tag{4.32}$$

However, only a portion of this power will be actually received by the radar, depending on the antenna's effective area, A_e, which is related to the antenna gain G_T by $A_e = G_T\lambda^2/4\pi$. Then:

$$P_R = P_D{}' A_e = \frac{P_T G_T^2 \sigma \lambda^2}{(4\pi)^3 \rho^4} \tag{4.33}$$

The RCS, σ, depends on various factors. Among these, the size of the object plays a significant role. Other factors include the material with which the target is made, the size of the target relative to λ, the incident and reflected angle, and the polarization of the radiation (both transmitted and received). Modeling the fragments as isotropic re-emitting spheres of size (diameter) s, and assuming that the ratio $s/\lambda \geq 0.2$ optical regime), the following relation holds [**]:

$$\sigma = \frac{\pi}{4} s^2 \tag{4.34}$$

while for smaller ratios (Rayleigh regime) we have:

$$\sigma = \frac{9\pi^5 d^6}{4\lambda^4} s^2 \tag{4.35}$$

and the radar cross-section value gives us a hint on the fragment size (see [23]). In other words, considering a radar network described by just one radar with given specifics: $\sigma = \sigma(s)$. We also have $\rho = \rho(h)$, as in the optical case.

A New Radar Weight

Assuming that all radars belonging to the network are able to detect $s_{min} = 15\ cm$ sized objects up to an altitude of $h_{max} = 2000\ km$ [††], we can:

[**]This is true for a wide range of applications. For instance, taking $s_{min} = 5\ cm$, the $s/\lambda \geq 0.2$ ratio condition holds true for Ka, Ku, X, C, S, and part of the L band.

[††]Similarly to what we have already mentioned in §, we stress that radar sensors are mostly employed to observe altitude shells up to 1000 km, as they suffer from rapid SNR degradation at higher altitudes ($SNR_{radar} \propto \rho^{-4}$) .

- compute the corresponding expected Signal to Noise Ratio for a given fragment of size s_{frag} at a given fragmentation altitude h_{frag}, $SNR_{radar}(s_{frag}, h_{frag})$;
- address its detectability, meaning check whether:

$$SNR_{radar}(s_{frag}, h_{frag}) > SNR_{radar}(s_{min}, h_{max}) \tag{4.36}$$

- in case the inequality holds true, compute the weight:

$$\omega_{radar} = 1 - \frac{SNR_{radar}(s_{frag}, h_{frag})}{SNR_{radar}(s_{min}, h_{frag})} \tag{4.37}$$

this is somehow analogous to the procedure presented in the optical case, where we stress the dependence on h_{frag} at the denominator, so as to ensure that $w_{radar} \in [0, 1]$.

As done earlier with the telescope case, we wrote a Python script to compute the radar weight associated with each fragment size, which is shown in Fig 4.8. Here, it is assumed that all radar sensors observe at a 30° elevation and that $s_{min,radar} = 15\ cm$ -sized objects are detectable at an altitude of $h_{max,radar} = 1500\ km$ (corresponding to $\rho_{max,radar} \sim 3110\ km$). Considering all other quantities in the radar SNR equation as constant, this amount to give a specific value for G_T and G_R. More specifically, the product of these two quantities gives a practical description of a telescope representing the network.

4.4 Threshold Size Evolution With Altitude

To have a better grasp on what we have just presented, it might be useful to show how the computed **threshold size** of a fragment - given by the limiting magnitude and the limiting signal in the optical and radar case respectively - **changes with the altitude**. As one can see from Fig. 4.7, the optical case is well fitted by a linear function, while in the radar case, a higher-order fit is needed. This is due to the different dependencies of $SNR_{optical}$ and SNR_{radar} from the range ρ. The radar's non-linearity is clearly linked to the fact that the radar signal behaves like ρ to the fourth power Referring to the brief explanation given in 4.3.2, this can be regarded as a consequence of the round trip of the pulse (to the target and back).

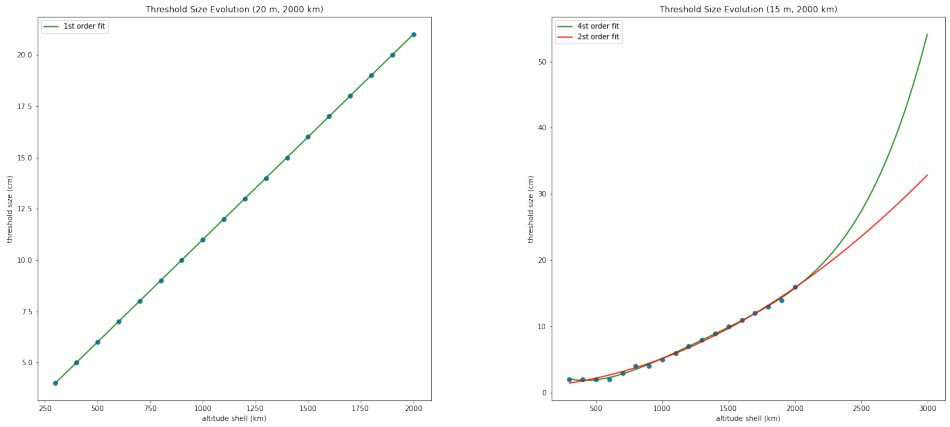

(a) Threshold size of a fragment vs altitude (optical case). **(b)** Threshold size of a fragment vs altitude (radar case).

Figure 4.7: Simulated ω-thresholds for the two different sensor types.

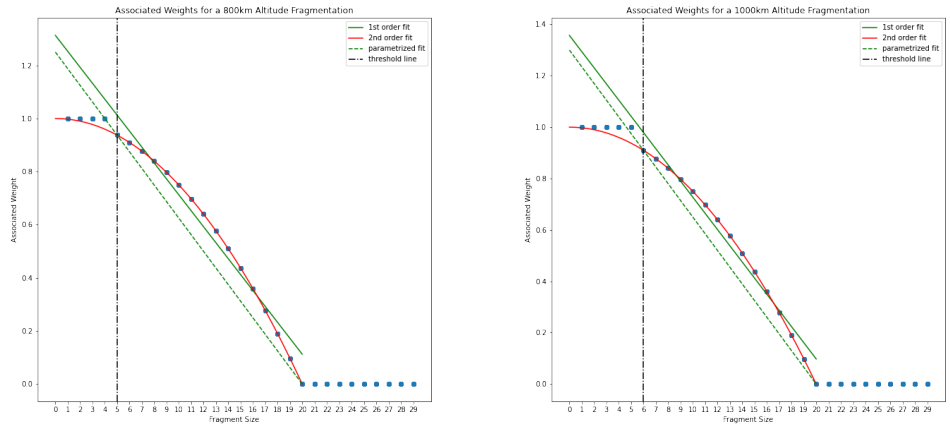

(a) Associated ω_{radar} weight for fragments up to 30 cm in an 800 km altitude orbit (radar case). **(b)** Associated ω_{radar} weight for fragments up to 30 cm in a 1000 km altitude orbit (radar case).

Figure 4.8: Simulated ω_{radar} weights for two different fragmentation cases. The middle part of the plot is well-fitted by a second-order polynomial red line). A first-order fit (green solid line) and the parametrized fit (green dotted line) performed as described above are also displayed.

5 Testing and Validation on Different Networks

We have developed a Python code to evaluate the FEI for different fragmentations in LEO, under specific assumptions on the available network. In particular, the code computes the evolution of the FEI across three distinct networks: **radar + optical, optical only, and radar only**. The case for which no sensor in the network is able to observe the fragmentation is also considered (this is of course the same as assuming **no network availability**). We presume that all networks have been previously optimized for statistical coverage, latitude and longitude distributions, scheduling, and other parameters that are challenging to model within the time frame of a Master's Thesis. Hence, we shall defer the resolution of such complexities to future works. In this context, we provide a concise yet exhaustive overview of the implemented program.

5.1 Inputs and Outputs

The program takes as **inputs**:

1. **the cloud files** generated by an *ad-hoc* software implementing the NASA breakup model [11]. E.g., for our tests the SDM software suite [8] was used. Other implementations of the NASA model (like, e.g., the MASTER software [24]) or other fragmentation models could of course be used to provide similar inputs.

   The fragmentation model shall provide a set of parameters needed for the index computation. Each text file, named *cloud_h_NNN* (where h is the fragmentation altitude in *km* and *NNN* is an integer number in the interval $t_0 < NNN < t_{end}$) contains, in order:

   - the epoch (in *Julian Days*)

- the fragment number k, $k = 1, 2, ..., N_{frag}$
- the fragment's area (m^2),
- the fragment's mass (kg)
- the fragment's orbital elements, in km and *degrees*;

2. **the sensors' elevation** ε (in *degrees*), assumed to be the same for every telescope or radar in the network. This assumption simplifies our model and algorithm, and it is justified for the reasons explained in Sec. 4.3.
3. **the minimum size** $s_{min,opt}$ of a fragment (in cm) observable with a telescope at the reference altitude (see next bullet) and the analogous $s_{min,radar}$ for the radar sensors;
4. **the maximum altitudes** $h_{max,opt}$ and $h_{max,radar}$ (in km) at which the smallest fragments $s_{min,opt}$ and $s_{min,radar}$ are detectable, both in the optical and radar case.

   Please note that assigning a tuple (s_{min}, h_{max}) is the same as providing an average performance for a given sensor. In the case of telescopes, for instance, assuming a very simple instrument model, this information could be exchanged with knowledge of the primary mirror diameter. Then, the diameter could be used as an input to the problem in place of (s_{min}, h_{max}). However, we assume the average "commercial" characteristics of a sensor are known and we stick with the choice of the tuple as an input to our model;
5. **the background population file**.

   This is given by the population model available at the fragmentation time t_{frag}, and contains orbital parameters and other information on the LEO-residing objects at a time right before the fragmentation epoch. Since the FEI measures the difference between the *post* and *pre* fragmentation environmental LEO risk, changing the background characteristics of the in-orbit population will also change the FEI. The background environment at an initial reference epoch is derived from the MASTER population, while the environment at different epochs in the future is obtained by evolving the MASTER population with the SDM model.
6. **the mean spatial density of objects in each** 50 km **altitude shell**, used to compute the fractional CSI as in [9].

The code can produce the following **outputs**:

1. **weight output files**, each containing, in order:
   - fragment size (in cm);
   - the final weight ω_{tr};
   - the optical weight $\mathcal{F}$;
   - the radar weight ω_{radar}.

2. **cloud CSI files**, applying the multiplicative factor ω_{tr} each containing:
   - the day (starting from the fragmentation epoch, as an *integer* from 1 to the final selected date, t_{end})
   - the cloud's CSI computed using $\omega_{tr} = min(\mathcal{F}, \omega_{radar})$ as a multiplicative factor. This is the case in a network where both types of sensors are available;

- the cloud's CSI computed using $\omega_{tr} = \mathcal{F}$ as a multiplicative factor, corresponding to the case of a network only made of telescopes;
- the cloud's CSI computed using $\omega_{tr} = \omega_{radar}$ as a multiplicative factor, for the case of a pure radar network.

3. **cloud CSI files, without applying the multiplicative factor**, i.e. assuming that no network is in place, and all fragments have $\omega_{tr} = 1$, containing:
   - the day (as an *integer* from 1 to t_{end})
   - the cloud's CSI summed over all N_{shells} shells, assuming no weighting factor is in place.

4. **Pre and Post - fragmentation CSI files**, for each day and altitude shell j. These are a number of LEO spherical shells of width L (in km) each (note that the width of the shell is a model parameter and is set to 50 km as a default value), with the first one starting at an altitude of 200 km and the last one ending at 2000 km. The FEI values are computed for each day in the interval $[1, t_{end}]$. The Pre- and Post-CSI files contain the values:
   - $\Xi_j(post)$ (optical and radar);
   - $\Xi_j(pre)$ (optical and radar);
   - $\Xi_j(post)$ (optical only);
   - $\Xi_j(pre)$ (optical only);
   - $\Xi_j(post)$ (radar only);
   - $\Xi_j(pre)$ (radar only).

   each computed as suggested in (3.12), applying the relative ω_{tr} to the CSI. If a mixed radar network is chosen, ω_{tr} is computed according to (5.1), while it amounts to (4.37)/(4.24) if the considered network is purely radar/optical.
5. **FEI files**, each containing the FEI value corresponding to altitude shells j.

5.2 The Algorithm

The software computes the optical and radar weights as defined in section (4.3). First, $\omega_{E_{RSO}}$ is calculated. As we've already mentioned , $\omega_{E_{RSO}} = \omega_{E_{RSO}}(s_{frag}, h_{frag})$, where $h_{frag} = a_{frag} - r_{\oplus}$, assuming each fragment to move in a **circular orbit** around the Earth. Since our model is currently designed for LEO, this simplifying assumption is justified. In case of fragmentations happening in highly elliptical orbits (e.g., Geostationary Transfer Orbits or Molniya orbits) the above assumptions should be changed. According to our $\omega_{AR}(h_{frag})$ definition (see Sec. 4.3.1), the collision altitude h_{frag} is the only parameter quantifying the Angular Rate of an object. Thus ω_{AR} is also readily obtained. Again, we stress that the circular orbits model, together with the assumption that the Angular Rate of an object as seen from the ground is the same for all fragments, are simplifying assumptions that have to

be properly justified and understood: it is clear that, given a collision, the fragments will, in general, distribute on orbits with eccentricities different from zero; moreover, the ω_{AR} so defined does not take into account any evolutionary effect in the fragments' semi-major axis, as it is assumed to be a function of the collision altitude only (recall (4.3.1)). Of course, the semi-major axis will in general change, - especially in cases where the atmospheric drag is more pronounced - but for the limited time frame of the analysis (typically limited to a few weeks-months) the approximation is justified. In a nutshell, as we stick to the original definition of ω_{AR}, the reader should just keep in mind that, for times far from t_0, ω_{AR} might not completely grasp the complex physics of the problem. Note that we performed some tests considering different values of the ω_{AR} parameter for each single fragment and checked that the results did not change significantly from those obtained with our main approach.
The two optical weights are then combined according to (4.24). As for the radar weight, ω_{radar} it is also easily computed using (4.37). The final weight, ω_{tr} associated to a given fragment is the **minimum** between the radar and optical contributions:

$$\omega_{tr} = min(\mathcal{F}, \omega_{radar}) \tag{5.1}$$

Next, the fractional CSI as in (3.3) is computed for all fragments, and it is multiplied by the fragment's ω_{tr}, according to (3.5):

$$\Xi_{k,j} = \Phi_{k,j} m_k \rho_j L_k f_k(i) \times \omega_{tr_k} \tag{5.2}$$

where $k = 1, 2, ..., N_{frag}$ indicates the fragment number.
Using the **shell index** $j = 1, 2, ... \frac{2000km - 200km}{L}$, the algorithm outlined so far acts on both the MASTER background population file - adding up the criticality given by each satellite on the j shell as it was prior to the fragmentation event and thus yielding the $\Xi_j(pre)$ values for each **object** k, and the generated collision files - adding up the information for each fragment k to give $\Xi_j(cloud)$. Considering equation (3.9), summing over all the fragments in the same shell, and finally dropping the "LEO" subscript to ease the notation, the algorithm computes the FEI as the ratio between:

$$\Xi_j(post) - \Xi_j(pre) = \Xi_j(cloud) - \Xi_{parent_j} \tag{5.3}$$

and $\Xi_j(pre)$:

$$\Xi_{FEI-PERC_j} = \frac{\Xi_j(post) - \Xi_j(pre)}{\Xi_j(pre)} = \frac{\Xi_j(cloud) - \Xi_{parent_j}}{\Xi_j(pre)} \tag{5.4}$$

in the above equation, Ξ_{parent} is the single fractional CSI of the intact parent object, prior to the fragmentation epoch.

5.3 Results

We simulated a collision between a 2000 kg upper stage (parent object) with orbital elements: $(a_p, e_p, i_p, \Omega_p, \omega_p, M_p)$ = (8178 km, 0.00003, 80.3°, 24°, 345°, 32°) and a 15 kg piece of debris, with a relative velocity of 10 km/s. The resulting debris cloud was propagated up to a time $t_{end} = 100$ days. We conducted simulations for four different fragmentation altitudes: $h_{frag} = 450$ km, 800 km, 1200 km, and 1800 km. In this discussion, we mainly present and analyze the results obtained for $h_{frag} = 450$ km and $h_{frag} = 1200$ km. We also incorporate relevant findings from the remaining fragmentation altitudes whenever they provide valuable insights. For our study, we chose to model a network employing radars to probe the Low Earth Orbit (LEO) environment up to 1200 km in altitude, and telescopes to detect objects at altitudes higher than 1200 km. In accordance with the definition of ω_{AR} (refer to section 4.3), this implies setting $\omega_{AR} = 0$ for our simulations. This division between radar vs optical regime reflects the current routine of the SST services. Indeed, radars demonstrate superior performances compared to telescopes at lower Low Earth Orbit (LEO) altitudes. However, their effectiveness is constrained by a limited range, as indicated by the relationship $SNR_{radar} \propto \rho^{-4}$. On the other hand, optical telescopes offer a cost-effective alternative for higher altitudes, where the use of very powerful (hence expensive) radars would be necessary.

5.3.1 450 km Altitude Fragmentation

First, we consider the 450 km altitude fragmentation. In order to analyze fragmentations of objects in space, one could decide to plot the apogee and perigee of fragments in relation to their orbital period. These plots go by the name of Gabbard diagrams and constitute a simple yet useful tool nowadays employed in virtually all satellite fragmentation studies (see Fig. 5.1). Upon collision or explosion, each individual fragment experiences changes in orbital energy, based on the amount and direction of Δv it receives. This can lead to an increase in apogee or a decrease in perigee. The altitude of the event influences the distribution of debris, forming an X shape with the center corresponding to the altitude/period of the object(s) at the event. The associated Gabbard diagram to the $h_{frag} = 450\ km$ fragmentation is shown in Fig. 5.1. The right-hand side of the diagram represents fragments that received a positive Δv, thus increasing their apogee altitude, while on the left-hand side are fragments with a negative Δv, thus decreasing their perigee altitude. Note that the left branches of the X are bent due to the effect of the atmospheric drag which tends to circularize the orbits and removes the fragments with perigee below about 200 km. Since we have $h_{frag} = 450km < 1200\ km$, we consider a pure radar network to be in place, with all sensors pointing at an elevation angle of 30°, due to the reasons explained in Sec. 4.3. One of this thesis's objectives is to address how the network's performance changes by changing its capabilities. As we mentioned in Sec. 5.2, our code can take the minimum detectable size, s_{min} of a fragment at a given altitude s_{max} as an input. The smaller this input size, the better the network. s_{min} is therefore a proxy for the network's capabilities. We considered, respectively: $s_{min} = 15$ cm, 10 cm, 5 cm at $h_{max} = 1200$ km for radar sensors. *

*These values may represent the capabilities of currently deployed radars used by various entities and companies worldwide for space surveillance and tracking. However, our code allows users to customize their choices for testing a specific network.

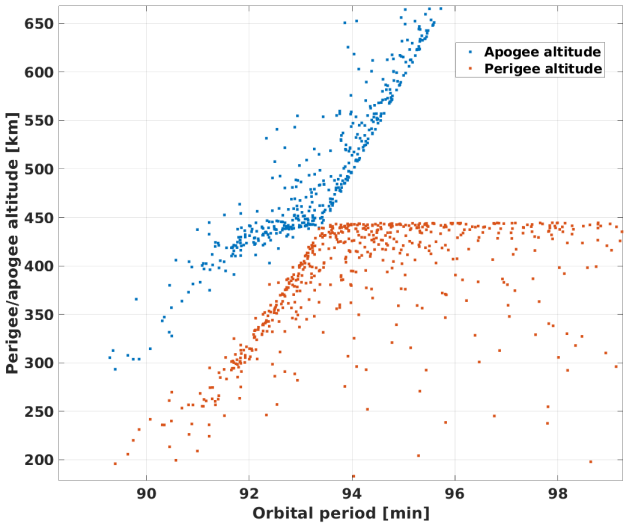

Figure 5.1: Gabbard diagram associated with the $h_{frag} = 450$ km fragmentation.

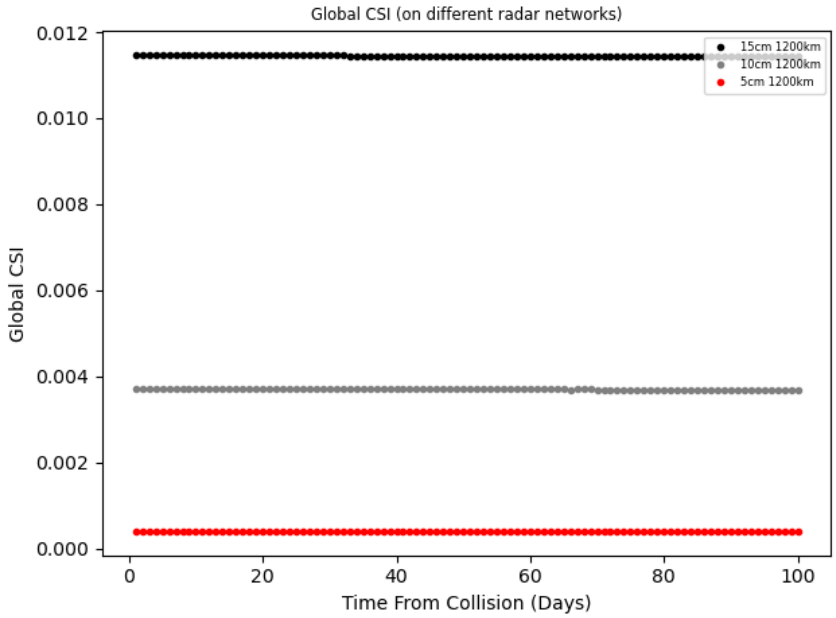

Figure 5.2: Global CSI associated with a $h_{frag} = 450\ km$ fragmentation as a function of time, for different radar networks.

Global CSI

In Figure 5.2 we show the computed effect of different networks on the computation of the overall LEO CSI (Global CSI) value as a function of time. This value decreases as the capability of the network increases, transitioning from radars with $s_{min} = 15\ cm$ to a network characterized by $s_{min} = 5\ cm$. At first glance, it might seem like the Global CSI values remain constant over time. However, a closer inspection shows how they monotonically decrease over time, due to the decaying of the fragments over time, caused by the atmospheric drag, given the low altitude of this event. Figure 5.3, which is a zoom-in on the red curve in 5.2, clearly illustrates this behavior for the network characterized by $s_{min} = 5\ cm$. Similar plots are obtained for the remaining two networks. The improvement provided by the network with $s_{min} = 5\ cm$ over the one with $s_{min} = 15\ cm$ is visually captured by Fig. 5.4, illustrating that the $s_{min} = 5\ cm$ radar network produces a CSI that is approximately $96\% - 97\%$ lower than the $s_{min} = 15\ cm$ network.

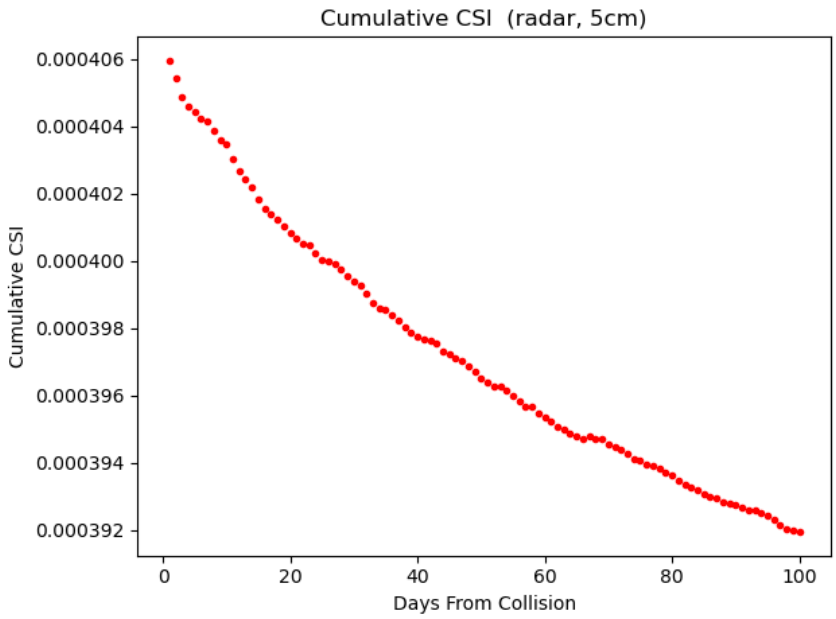

Figure 5.3: The same as Fig. 5.2, but limited to the $s_{min} = 5$ cm case (red line in Fig. 5.2).

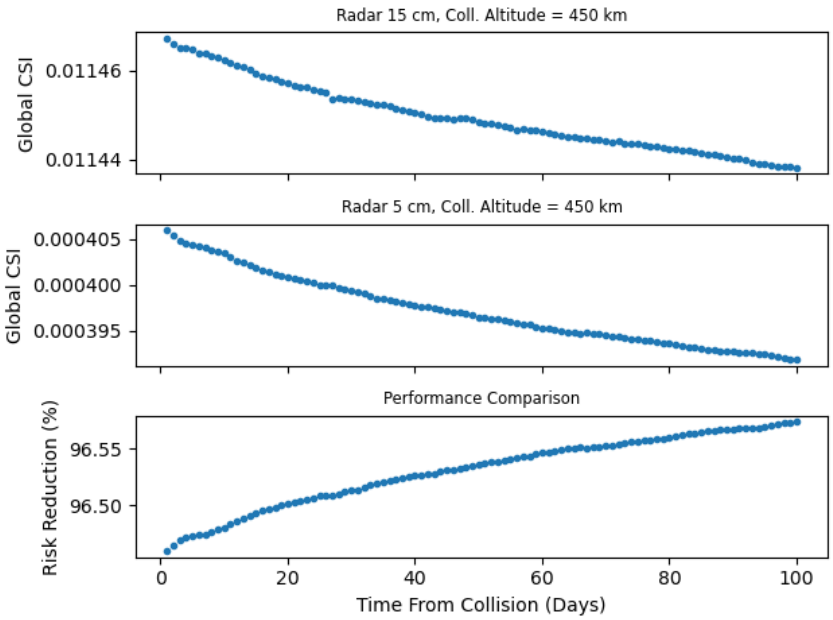

Figure 5.4: Comparison of Global CSI values as given by two different networks. Top: network with $s_{min} = 15\ cm$; middle: network with $s_{min} = 5\ cm$; bottom: percentage ratios between the two produced CSIs.

Cloud CSI

It is also interesting to take a look at the cloud's contribution to the Global CSI we obtained. In this regard, Figure 5.5 provides a clear explanation. The cloud contributions for the three different networks are compared. For reference, we also plot (blue dots) the Cloud's CSI values in the scenario where no fragment is detectable (i.e., the blue dots correspond to the case where all fragments have $w_{radar} = 1$). As expected, this last case is by far the most critical. Fortunately, dedicated radars are distributed worldwide, making the actual CSI values of a potential future fragmentation much more similar to those represented by the lowest sets of dots.

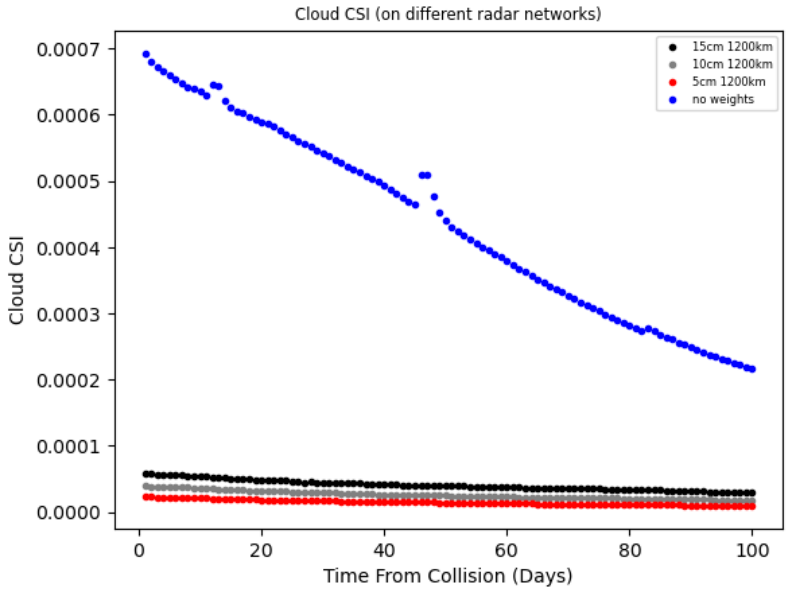

Figure 5.5: Cloud's CSI contribution as computed using weights associated to different radar networks. The blue dots correspond to the case in which no network is in place, and all fragments are associated with a maximum weight of 1.

Based on the information in Fig.5.5, it is evident that an improvement in network capability results in a reduction in the Cloud's CSI value. It is noteworthy that, with the advancement of the network, the cloud's influence on Global CSI becomes more significant. This is demonstrated in Figure 5.6, where we observe approximately a 6% contribution of clouds to the overall Low Earth Orbit (LEO) criticality in the case of a radar network described by $s_{min} = 5$ cm, one day after the fragmentation epoch. In contrast, contributions for other networks consistently remain below this percentage value—approximately 1% at $s_{min} = 10$ cm and around 0.5% at $s_{min} = 10$ cm. This can be explained by the fact that a more advanced network is more sensitive to changes in the environment, making a specific cloud more noticeable. Further support for this explanation comes from noticing how the cloud's contribution to the Global CSI is nearly zero in the case when $w_{radar} = 1$ (represented by the blue dots). In this scenario, the CSI associated with the background is very high, and the cloud's contribution becomes almost indistinguishable within it.

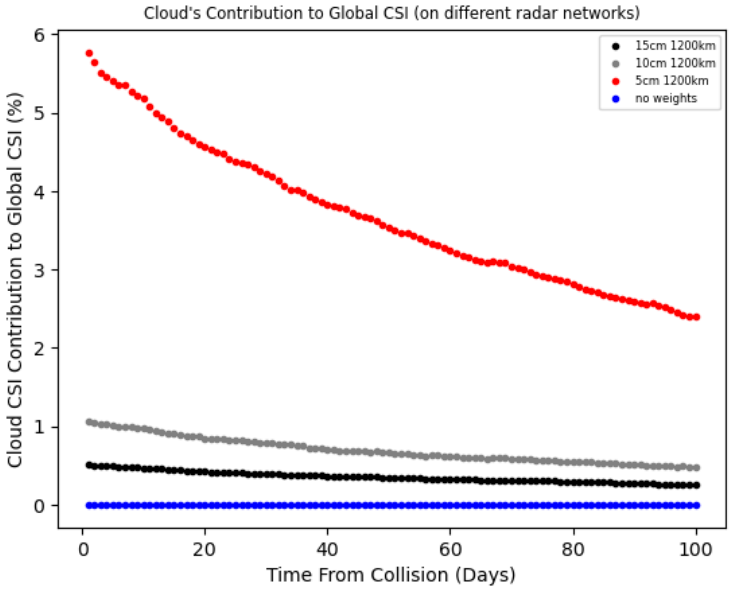

Figure 5.6: Debris cloud's contribution to the global CSI, for different networks. The blue dots correspond to the case where the same maximum weight of 1 is assigned to all fragments.

FEI

The computation of the FEI, performed as discussed in Section 4, yielded the results shown in Figure 5.7 and Figure 5.8. The first plot displays the percentage FEI given by (3.14) on the $s_{min} = 5\ cm$ network, respectively at 1 (solid line) and 100 days (dotted line) after the fragmentation event. Although the percentage FEI effectively identifies altitudes experiencing significant stress from fragmentation, it lacks the ability to convey the magnitude of the difference between pre-and post-fragmentation. It is possible for two distinct fragmentations, characterized by different values of Ξ_{pre} and Ξ_{post}, to result in the same $\Xi_{FEI-PERC}$ ratio. This similarity arises because the denominator serves as a normalization factor, preventing a clear understanding of the magnitude of the numerator. In order to solve this degeneracy, we also compute the values of (3.13) and plot them in Figure 5.8. In this second plot, it is evident that the lowest LEO shells are characterized by a very low FEI, indicating that the difference between the post-fragmentation and pre-fragmentation situations is very small. By multiplying the two functions to keep track of the magnitude of the FEI as defined by the differences only, we arrive at Figure 5.9, which indeed showcases a prominent bump corresponding to the relevant fragmentation altitude. All three images provide an insight into how the FEI evolves over time.

A robust environmental index should also effectively capture the overall risk at a specific time, essentially tracking the cloud as it propagates and spreads within the LEO region. Observing the Modulated FEI plot in Figure 5.9, it is evident that there is an approximately four-order-of-magnitude difference between its values at $t = 1\ Day$ and $t = 100\ Days$ in the lowest altitude shells — those between 200 km and 400 km. This difference is interpreted as the impact of atmospheric drag, which acts as a sink for all fragments, especially for those in the low-LEO altitude range. Many fragments are dragged to lower altitudes, effectively reducing the FEI over a 100 - days period. Higher altitudes are less affected by this evolutionary phenomenon.

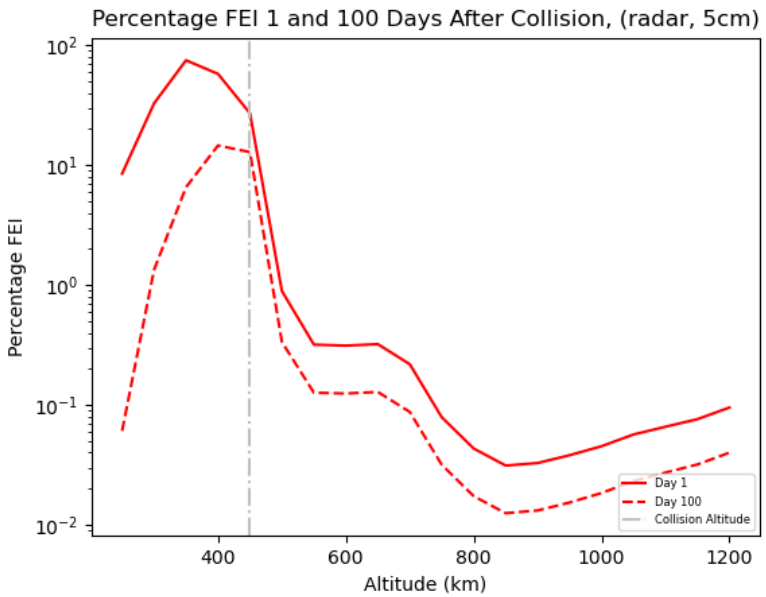

Figure 5.7: Percentage FEI as computed on a network characterized by $s_{min} = 5\ cm$ at an altitude of $h_{frag} = 450\ km$

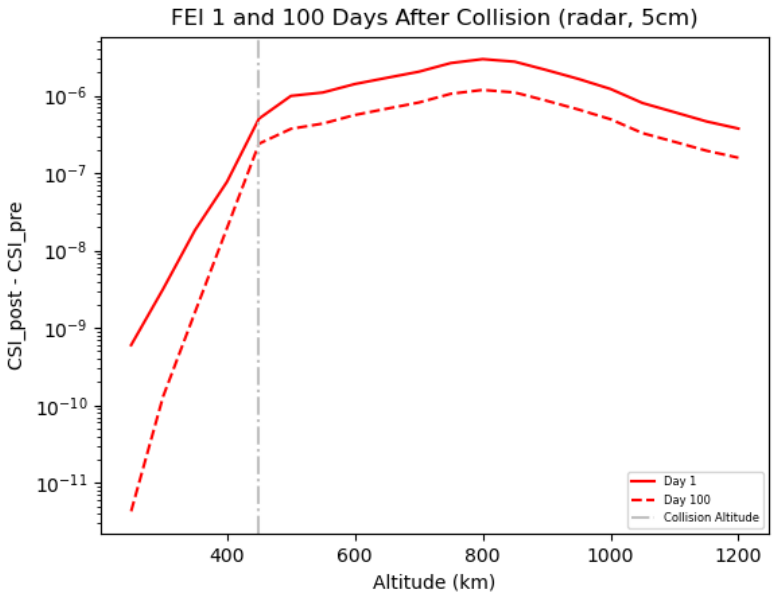

Figure 5.8: FEI as computed on a network characterized by $s_{min} = 5\ cm$ at an altitude of $h_{frag} = 450\ km$.

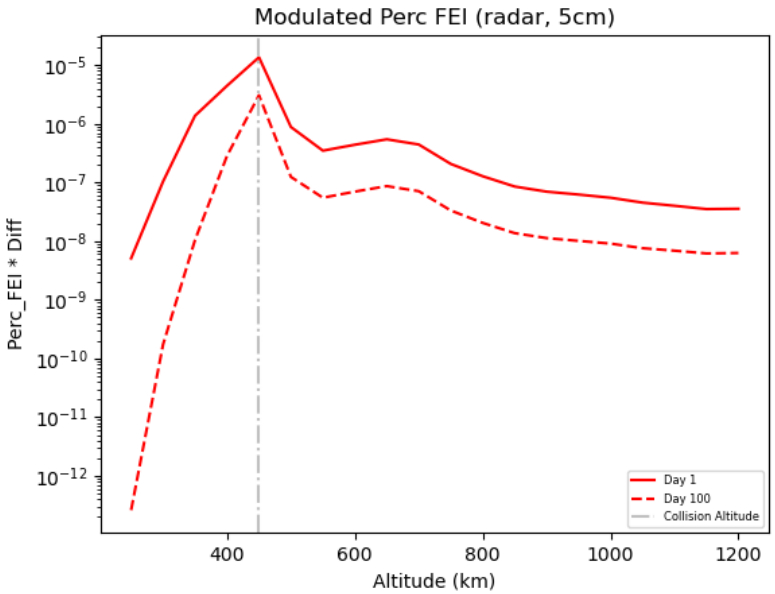

Figure 5.9: Plot showing the product between the FEI and the Percentage FEI values, as computed on a network characterized by $s_{min} = 5\ cm$ at an altitude of $h_{frag} = 450\ km$.

5.3.2 1200 *km* Altitude Fragmentation

We now move to the fragmentation happening at our assumed radar observation limit[†], characterized by $h_{frag} = 1200\ km$. At this regime, we discard radars and switch to an optical network. Three different optical networks, characterized by $s_{min} = 20$ cm, 15 cm, 5 cm at a maximum altitude of $h_{max} = 2000$ km have been tested. All telescopes are assumed to have a 30° elevation.
As already done for the $h_{frag} = 450$ km event, we include here the useful Gabbard diagram associated with this fragmentation (see Fig. 5.10).

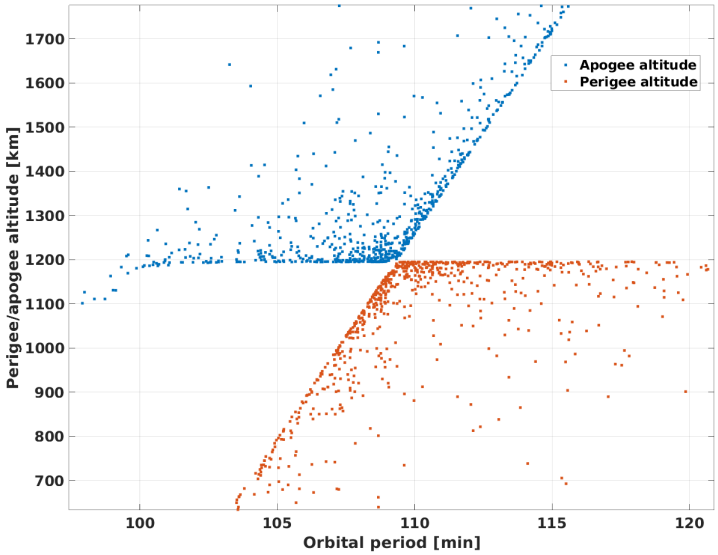

Figure 5.10: Gabbard diagram associated with the $h_{frag} = 1200\ km$ fragmentation.

Global CSI

As observed in Figure 5.11, the influence of various networks on the overall CSI evolves similarly to what we have previously discussed for the 450 km fragmentation. The global CSI value decreases as the network's sensitivity increases, transitioning from telescopes with $s_{min} = 20$ cm to a network characterized by $s_{min} = 5$ cm. Figure 5.12 specifically highlights this behavior for the network with $s_{min} = 20$ cm, and analogous patterns emerge for the remaining two networks. The Cumulative Cloud CSI plot is remarkably different than the one previously shown for a 450 *km* fragmentation, as a small increase (of the order $\sim 10^{-5}$) can be observed in the cloud's CSI, up to 40 days after the fragmentation epoch. The behavior depicted in Fig 5.12 is most likely a consequence of the complicated interplay between 1) the breakup model used and 2) the evolutionary dynamics of fragments

[†]We remember that the limiting altitude is a model parameter and we note that in the operational environment within, e.g., the US surveillance network, very powerful radars are used even above this 1200 km limit, used here as a test value.

spreading the cloud of fragments over different altitude bands.
The enhanced performance of the $s_{min} = 5$ cm telescope network is again visually captured in Fig. 5.13, indicating a CSI approximately 95% lower than the $s_{min} = 20\ cm$ network.

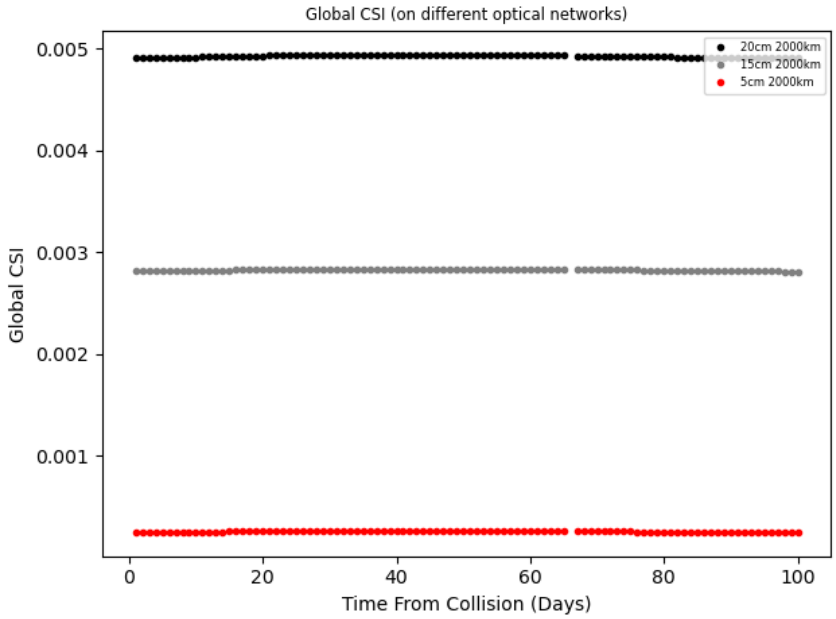

Figure 5.11: Global CSI associated with a $h_{frag} = 1200\ km$ fragmentation as a function of time, for different optical networks.

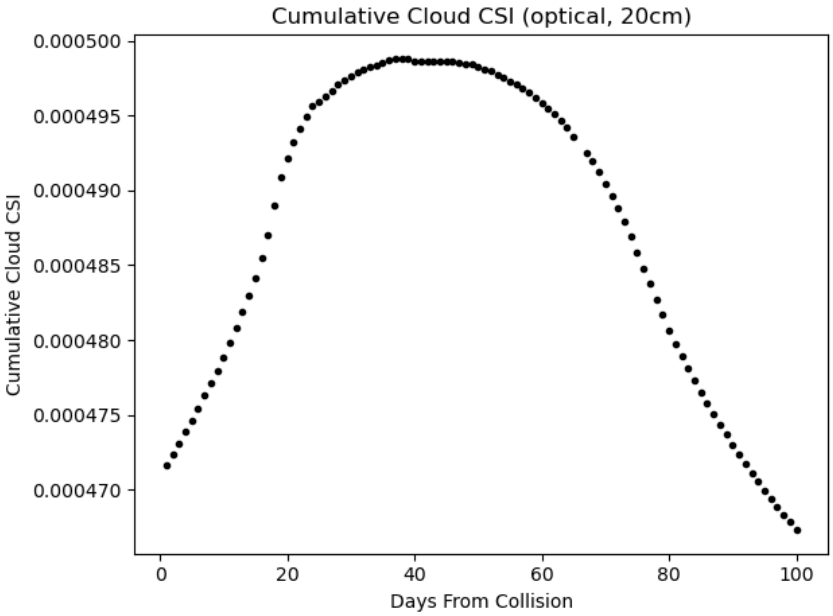

Figure 5.12: The same as Fig. 5.11, but limited to the $s_{min} = 5$ case (black line in Fig. 5.11).

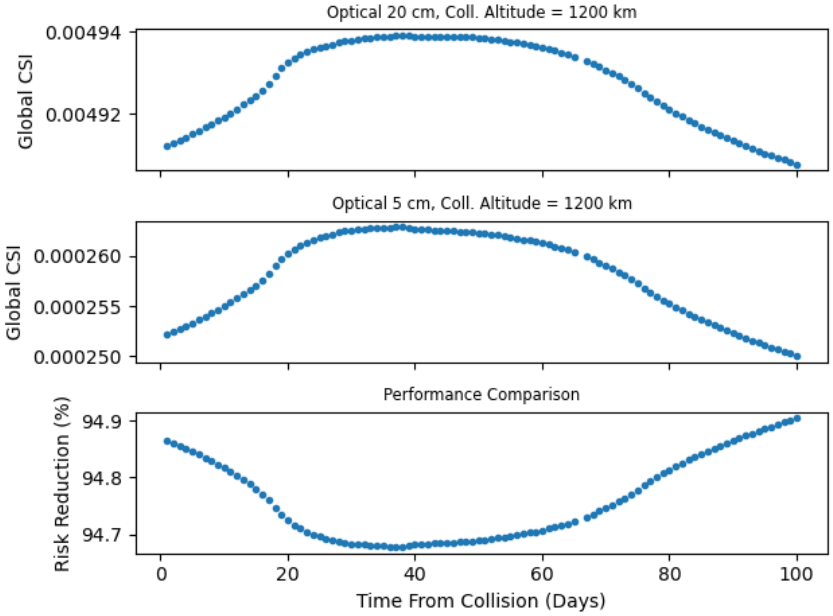

Figure 5.13: Comparison of Global CSI values as given by two different optical networks. Top: network with $s_{min} = 20\ cm$; middle: network with $s_{min} = 5\ cm$; bottom: percentage ratios between the two produced CSIs are plotted.

Cloud CSI

The plots depicting the CSI evolution exhibit a general pattern consistent with those previously presented for the $h_{frag} = 450$ km fragmentation. The highest Cloud's CSI values are observed when all fragments are given equal weight ($w_{tr} = 1$), decreasing as the optical network's performance improves (refer to Fig. 5.14). However, the most intriguing result is illustrated in Fig. 5.15. Notably, the $s_{min} = 5$ cm optical network demonstrates remarkable sensitivity, with the cloud accounting for a significant 70% of the globally computed CSI. In contrast, lower values of $10\% - 15\%$ are observed for less powerful networks, with the percentage decreasing as the sensor's capability diminishes.

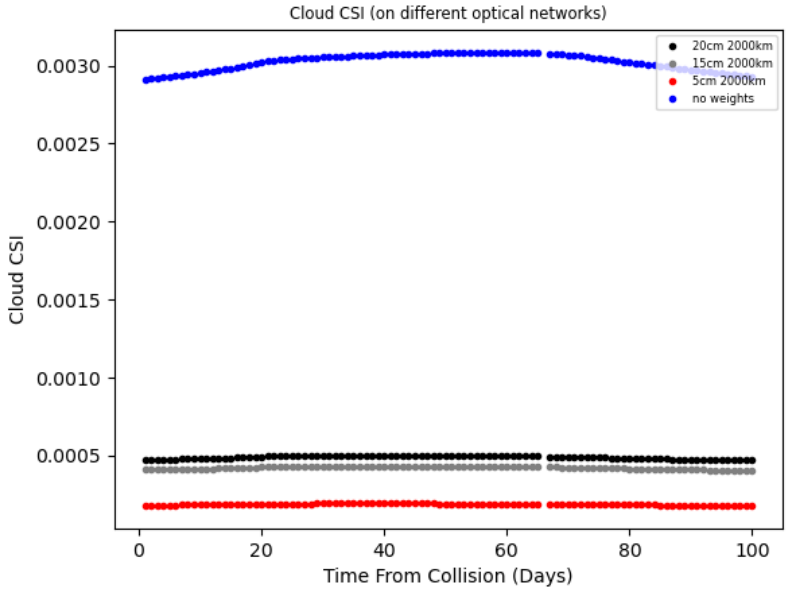

Figure 5.14: Cloud's CSI contribution as computed using weights associated to different optical networks. The blue dots correspond to the case in which all fragments are associated with a maximum weight of 1.

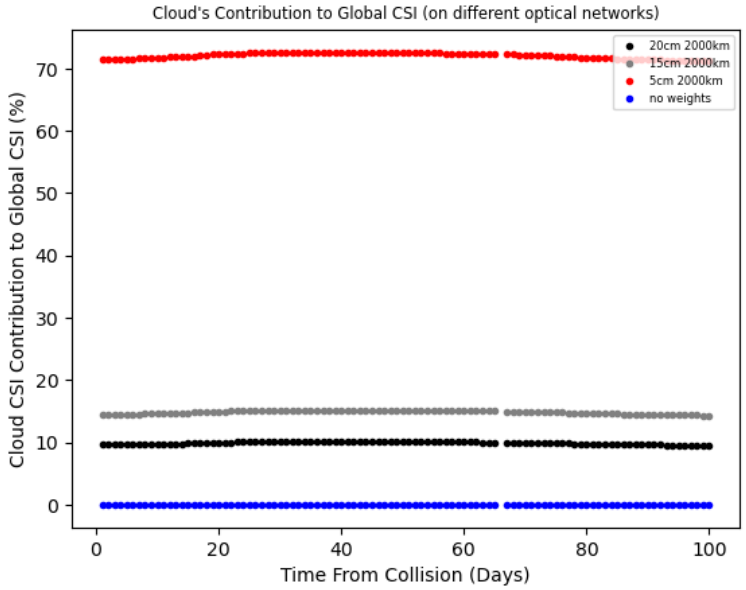

Figure 5.15: Debris cloud's contribution to the global CSI, for different networks. The blue dots correspond to the case where the same maximum weight of 1 is assigned to all fragments.

FEI

The FEI plots (5.16, 5.17, 5.18) showcase once again the ability of the index to localize the altitude shells that are most interested by a fragmentation (in this case, $h_{frag} = 1200\ km$). The atmospheric drag effect at high altitudes is very inefficient. For this reason, no relevant change in the FEI is observed at day 100 with respect to day 1.

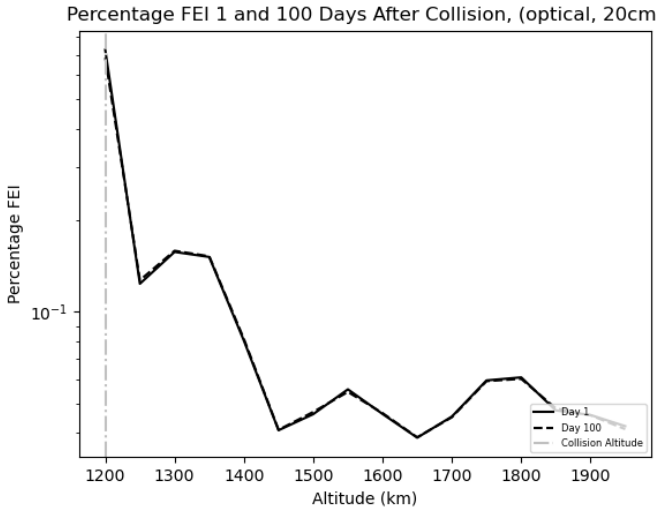

Figure 5.16: Percentage FEI as computed on a network characterized by $s_{min} = 20\ cm$ at an altitude of $h_{frag} = 1200\ km$

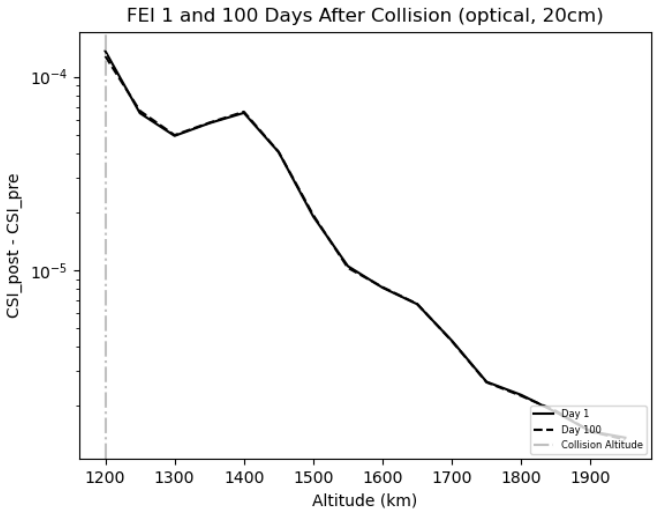

Figure 5.17: FEI as computed on a network characterized by $s_{min} = 20\ cm$ at an altitude of $h_{frag} = 1200\ km$.

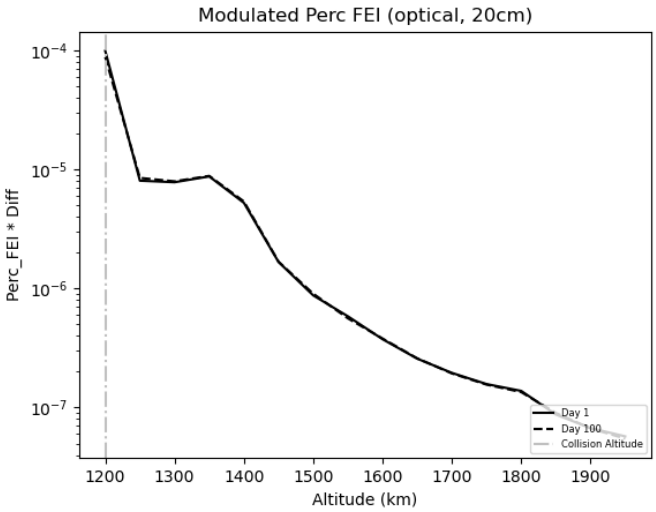

Figure 5.18: Plot showing the product between the FEI and the Percentage FEI values, as computed on a network characterized by $s_{min} = 20\ cm$ at an altitude of $h_{frag} = 1200\ km$.

We obtained similar plots for the fragmentations at $h_{frag} = 800\ km$ and $h_{frag} = 1800\ km$. Given that they basically share the same trends and show the same results as the two already discussed cases, it is not considered necessary to present them here, so as not to overload the attention of the reader.

In conclusion, our results show how the improved FEI is capable of characterizing the risk posed by fragmentation on a given network of sensors. Additionally, it identifies specific altitude shells that are expected to be particularly affected by the debris cloud in the short term.

6

A Dynamical Indicator for Decision Makers

In the previous chapter, we characterized the impact of fragmentation on specific surveillance sensors, and we did so using the optical and radar *SNR* as a risk metric. In other words, we performed what we could call a **"network-related" characterization**. However, a debris cloud is a **dynamical object** and - as such - evolves over time, according to the gravitational forces acting on the single fragments (the non-gravitational perturbations are usually significantly lower in magnitude and are therefore neglected in our analysis). Immediately following a fragmentation, all fragments are found in the surroundings of the collision or breakup location, and an ellipsoidal distribution of fragments can be observed in the Cartesian coordinate space. However, different fragments are characterized by different velocities, distributed according to how the breakup energy is shared among them. Due to the ΔV imparted to the fragments by the fragmentation energy, their orbital elements are changed from the ones of the parent object. In particular, the semi-major axis and the eccentricity get a significant modification, while the inclination is more difficult to modify (unless the fragmentation happens very close to an orbital node). Due to the change in semi-major axis and eccentricity, the fragments follow orbits with different orbital periods. Therefore, at some later time, the initial ellipsoid is stretched and the fragments fill a ring around the orbit of the parent object, encircling the Earth. During this phase, which lasts only a few orbits, orbital perturbations due to the non-spherical shape of the Earth are negligible, allowing for the application of the two-body problem equations to study the system's dynamics. The orbital parameters of the fragments are often assumed to remain constant in this phase, lasting only a few orbits. In the absence of perturbations, the fragments would retain a ring-like configuration, defined by a point known as the **pinch point**, where all fragments converge, corresponding to the breakup location [25]. However, in the subsequent phases, the Earth's **oblateness** (measured by the quadrupole term of the expansion of the gravity potential in terms of spherical harmonics, J_2) alters this geometry and the related perturbations gain significance, inducing **nodal and apsidal precession** in the orbits. The **longitude of the ascending node (LAN)**, Ω, and the **arguments of periapsis**, ω, evolve over time at rates contingent upon the orbital parameters of the fragments (e.g., [25]). As in the previous phase, each fragment possesses distinct orbital parameters, resulting in varying rates of orbit modification. Consequently, the pinch point disperses; the

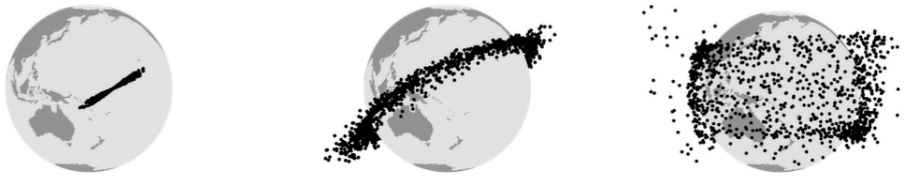

(a) Ellipsoid **(b)** Toroid **(c)** Band

Figure 6.1: Phases of debris cloud evolution as classified by [3]. Credits: [4]

progression of ω transforms the ring into a flat torus, spanning the range between the smallest perigee and the largest apogee. Additionally, the diffusion of Ω spreads the thorus creating a band around Earth, delimited in latitude by the inclination of the parent orbit (see Fig. 6.1). As the J_2 term exerts varying influences on orbits with differing inclinations, the duration of this transition can range from several months to several years, depending on the object's configuration at the time of fragmentation. In other words, if we refer to the phase where fragments are all clustered in a small ellipsoid, so as to be able to somehow treat the ellipsoid's orbit (considered as a point) via a set of given orbital elements, and if we call this a "**post-fragmentation orbit (PFO)**", there will then be some specific post-fragmentation orbits for which the J_2 **effect** is the most pronounced. This implies that the fragments will disperse in the shortest time-span for these particular cases, and the **randomization process** of the orbital elements **will be shorter**. Then, considering and comparing the timescale of this process for a variety of different PFOs, would lead to a more **"dynamical" characterization** of the risk for a given asset associated with the fragmentation, and to the definition of an indicator which, as we shall see, might be employed as a useful tool for decision-makers. Namely, the purpose of the $J2$ indicator shall be to quickly alert an operator if a spacecraft will be affected by a given fragmentation and the time frame for such interaction. We will refer to it as "$J2$ indicator", Υ.

6.1 The J_2 Term

Even though their geometry can be approximated to a sphere, celestial objects possess an irregular shape. For this reason, the potential appearing in the well-known Poisson equation:

$$\nabla^2 V = 4\pi\gamma\rho \tag{6.1}$$

(where V is the body's gravitational potential, γ is the gravitational constant, and ρ the mass density at each point, $\rho = 0$ for vacuum), will in general deviate from the purely spherical one. Specifying the Poisson's equation in the vacuum leads to the Laplace equation:

$$\nabla^2 V = 0 \tag{6.2}$$

whose solution in spherical coordinates (r, θ, φ) is a cylindrically-symmetric potential of the form:

$$V(r,\theta) = -\frac{GM}{r}\left[1 - \sum_{n=2}^{\infty} J_n \left(\frac{R^n}{r}\right) P_n(\cos\theta)\right] \tag{6.3}$$

In this equation, $P_n(\cos\theta)$ are the Legendre Polynomials, R is the object's equatorial radius, and J_n are the gravitational moments determined by the values of V at the object's surface, defined as:

$$J_n = -\frac{1}{mR^n}\int_0^R \int_{-1}^1 r^n P_n(\cos\theta)(r,\cos\theta)2\pi r^2\, d(\cos\theta)dr \tag{6.4}$$

The J_n terms describe the object's shape. More specifically, J_2 contains information on its flattening due to rotation. Keeping the J_2 term only, one finds:

$$V(r,\theta) = -\frac{GM}{r}\left[1 - J_2\left(\frac{R}{r}^2\right)P_2(\cos\theta)\right] \tag{6.5}$$

In terms of the dynamics of the system, we then have:

$$\ddot{r} = -\nabla V = -\nabla(U+\mathcal{R}) \tag{6.6}$$

with U the Newtonian potential and $\mathcal{R}$ a **disturbing potential function** due to J_2. $\mathcal{R}$ can be expressed in terms of the object's orbital elements and, therefore, it can be used in the **Lagrange Planetary Equations** to compute the changes in the osculating orbital elements due to the J_2 term:

$$\begin{aligned}
\frac{da}{dt} &= \frac{2}{na}\frac{\partial\mathcal{R}}{\partial\lambda}\\
\frac{de}{dt} &= -\frac{\sqrt{1-e^2}}{na^2e}\left(1-\sqrt{1-e^2}\right)\frac{\partial R}{\partial\lambda} - \frac{\sqrt{1-e^2}}{na^2e}\frac{\partial\mathcal{R}}{\partial\omega}\\
\frac{di}{dt} &= -\frac{\mathrm{tg}(i/2)}{na^2\sqrt{1-e^2}}\left(\frac{\partial\mathcal{R}}{\partial\lambda}+\frac{\partial\mathcal{R}}{\partial\omega}\right) - \frac{1}{na^2\sqrt{1-e^2}\sin i}\frac{\partial\mathcal{R}}{\partial\Omega}\\
\frac{d\Omega}{dt} &= \frac{1}{na^2\sqrt{1-e^2}\sin i}\frac{\partial\mathcal{R}}{\partial i}\\
\frac{\partial\omega}{\partial t} &= \frac{\sqrt{1-e^2}}{na^2e}\frac{\partial\mathcal{R}}{\partial e} + \frac{\mathrm{tg}(i/2)}{na^2\sqrt{1-e^2}}\frac{\partial\mathcal{R}}{\partial i}\\
\frac{d\lambda}{dt} &= n - \frac{2}{na}\frac{\partial\mathcal{R}}{\partial a} + \frac{\sqrt{1-e^2}\left(1-\sqrt{1-e^2}\right)}{na^2e}\frac{\partial\mathcal{R}}{\partial e}
\end{aligned} \tag{6.7}$$

If the object's orbit is not highly eccentric the disturbing potential only depends on i, e and a and, as a consequence, $\dot{a},\dot{e},\dot{i}=0$. This implies that the shape of the orbit does not change while its orientation in space can, since both the derivative of the perigee argument ω and the longitude of the ascending node Ω are not zero according to (6.7). From the above equations and the form of the disturbing function, it can be shown that:

$$\begin{aligned}
\dot{\omega} &= \frac{3}{2}nJ_2\left(\frac{R}{a}\right)^2\frac{\left(2-\frac{5}{2}\sin i\right)}{\left(1-e^2\right)^2}\\
\dot{\Omega} &= -\frac{3}{2}nJ_2\left(\frac{R}{a}\right)^2\frac{\cos i}{\left(1-e^2\right)^2}
\end{aligned} \tag{6.8}$$

According to the last Lagrange equation also the mean longitude λ, the sum of the RAAN, the argument of perigee, and Mean Longitude angles ($\lambda = \Omega+\omega+\mathcal{M}$) changes with time because of the J_2 perturbation since it

depends on the partial derivatives of the disturbing functions with respect to a and e. This means that the satellite will pass by a given true anomaly at a slightly different time.

6.2 The J_2 Indicator

Given section 6.1's premises, we could try to quantify how quickly the fragments are spreading in the given fragmentation shell. For instance, according to eq. (6.8) in the previous discussion, a fragmentation in polar orbit has a spreading of the orbital nodes under the effect of the J_2 perturbation, slower than a similar event in a quasi-equatorial orbit. In general, the more eccentric the orbit, the more prominent the variation of the RAAN. However, we will assume a **circular post-fragmentation orbit**. In the LEO region, the effect is of some $10 - 20°/day$. Figure 6.2) qualitatively highlights the effect for both $\dot{\omega}$ and $\dot{\Omega}$.

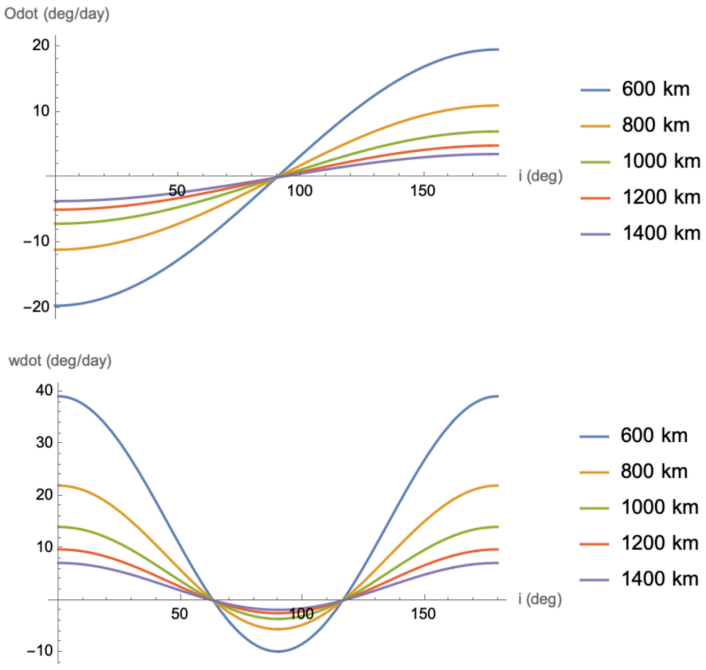

Figure 6.2: Ω (top) and ω (bottom) variations due to the J_2 term for a LEO satellite orbiting at different altitudes.

Spreading Timescale

A **timescale** for the spreading process (and relative band formation) can be defined as the time it takes for the fastest fragment to catch up with the slowest one, in terms of nodal/apsidal rate. Indeed, both the apsidal and nodal dispersions are considered to be completed when that occurs. Various definitions of the T_Ω and T_ω timescales can be found in the literature. Some, like in [25], rely on the knowledge of the semi-major axis of the fastest and

slowest fragments after the fragmentation. In that case, the proposed band formation period is:

$$T_{\Omega}^{Ch} = \frac{\pi}{|\dot{\Omega}_{+} - \dot{\Omega}_{-}|}, \; T_{\omega}^{Ch} = \frac{\pi}{|\dot{\omega}_{+} - \dot{\omega}_{-}|} \tag{6.9}$$

Others, like [26], have tried to give estimations only based on the parent object's initial orbit:

$$T_{\Omega}^{As} = \frac{\pi}{2|\delta\dot{\Omega}_{max}|}, \; T_{\omega}^{As} = \frac{\pi}{2|\delta\dot{\omega}_{max}|} \tag{6.10}$$

where $\delta\dot{\Omega}_{max}$ and $\delta\dot{\omega}_{max}$ are the estimated nodal and apsidal rates, found using the Gauss's equations relating the velocity variation to the variation of the orbital parameters. The two rates are a function of β, the out-of-plane angle of the velocity imparted to the fragment, Δv, the parent's orbit inclination i, the argument of latitude $u = \omega + \nu$, whee ν is the true anomaly, and the parent's orbit semi-major axis, a:

$$\delta\dot{\omega}_{max} \sim -\frac{3}{2} J2 \frac{r_{\oplus}^2}{a^3} [\, (\, 2 - \frac{5}{2} \sin i^2) \, \cos\beta + \frac{5}{2} \sin 2i \cos u \sin\beta] \, \Delta v$$

$$\delta\dot{\Omega}_{max} \sim -\frac{3}{2} J2 \frac{r_{\oplus}^2}{a^3} (\, 7 \cos i \cos\beta + \sin i \cos u \sin\beta) \, \Delta v$$

Please note that, if the velocity variation (given by the fragmentation) is much lower than the orbital speed v_0 - as it is the case for weak, isotropic, and non-catastrophic explosions or collisions - then the PFO can be assumed to coincide with the parent's orbit at the time of fragmentation, and Ashenberg's formulation, in Eq. 6.10, holds. In more complex cases, one might turn to Chobotov's formulation as in Eq. 6.9. A brief review of the suggested timescales can be found in [4], where it is also pointed out how both Chobotov's and Ashenberg's estimates - (6.9) and (6.10) - actually underestimate the band formation timescale. This is due to the fact that, both in [25] and [26] computations, the band formation period is defined as the time required by the difference in the nodal/apsidal rate to cover an angle of π instead of 2π. This assumption was tested and it was verified that only an incomplete band is obtained in this way. For this reason, [4] proposes the following:

$$T_b = 2 \times max(T_{\Omega}^{As}, T_{\omega}^{As}) \tag{6.11}$$

Nevertheless, upon performing a more detailed examination of the cloud's numerical propagation it was shown [4] that it might be useful to opt for a more conservative approach and choose

$$T_b = N_{sf} \times max(T_{\Omega}^{As}, T_{\omega}^{As}) \tag{6.12}$$

where the safety factor N_{sf} is adopted to allow for a T_b computation that does not require a continuous check of the cloud's uniformity state during the propagation. A value $N_{sf} = 3$ was chosen in [4], and we adopt the same value here. In other words, choosing $N_{sf} = 3$ ensures that the cloud had enough time to spread uniformly in the space surrounding the Earth.

It is interesting to observe that Ashenberg's formulation also assigns a finite time for the band formation in the

following cases:

$$i = \arcsin\left(\frac{2\sqrt{5}}{5}\right),\ i = \frac{\pi}{2} \tag{6.13}$$

respectively corresponding to the critical inclination for which we have:

$$\dot{\omega} = 0,\ \dot{\Omega} = 0 \tag{6.14}$$

in equations (6.8). This holds because any fragmentation will induce an out-of-plane component that results in an inclination change, and this will happen for every fragment. In this sense, a fragmentation characterized by an infinite T_b can be ruled out. Nevertheless, it might worth checking which conditions on the orbital elements yield the longest T_b, which we will call T_0, and using this as a normalization factor to define:

$$\tau = \frac{T_b}{T_0} \tag{6.15}$$

Given these premises, it looks like it would be safe to choose either $T_b(i = \arcsin\frac{2\sqrt{5}}{5})$ or $T_b(i = \frac{\pi}{2})$ as the normalization timescale T_0 appearing in the τ definition. However, the presence of these two relative maxima in the T_b function makes things less trivial: other considerations have to be done before rushing into a mathematical definition of τ. For instance, a dispersed cloud, while detrimental for a whole altitude band, due to the dilution might lower the risk of catastrophic collisions on a given asset. On the other hand, the risk is enhanced in the presence of a cloud with a great spatial density whenever out asset is crossing the cloud itself. Exploring the pre-fragmentation conditions of the parent object's orbital elements - such as inclination - can reveal if certain factors contribute to spatial density peaks within the cloud. Previous research, like [27], illustrates that fragmentations occurring in polar orbits exhibit significant spatial density at the polar nodes due to orbital plane spreading. Over time, the precession of the pinch point towards these nodes makes those regions more crowded. As we will also see in section 6.4.1, this situation is especially hazardous to those assets in **high inclination orbits**.

For this reasons, we will set $T_0 = T_b(i = \frac{\pi}{2})$. However, it is worth noting that - due to the presence of the other T_b peak at $i = \arcsin\left(\frac{2\sqrt{5}}{5}\right)$ - ω_{J2} is not a monotonically decreasing or increasing function of the inclination, meaning that different pre-fragmentation conditions (e.g. differences in inclination) might yield similar values of the J_2 indicator associated with a given asset.

In any case, it is evident that certain combinations of orbital elements, corresponding to specific orbits, can heighten the risk for nearby assets. This will in general depend on:

1. the cloud's dispersion timescale, T_b;
2. the fraction (or percentage) f_{cloud} of cloud debris that could potentially interest the asset, meaning those characterized by $r_{p,sat} < a_{fragment} < r_{a,at}$, where $r_{p,sat}$ and $r_{a,at}$ are respectively the asset's perigee and apogee. This, in turn, will depend on the relative asset-fragment distance in the orbital elements space (assuming the asset to be on an orbit with inclination $i_0 = i_{PFO}$, f_{cloud} will highly depend on the relative asset-fragment semi-major axis);
3. the amount of time $\mathcal{T}$ spent by the asset in the critical post-fragmentation regions.

Item 3) implies that no risk is posed by the fragmentation on the asset when the satellite is in an orbit that has a null intersection with the cloud. This is the case, for instance, of HLEO satellites whenever a fragmentation in LLEO happens: the big difference in the semi-major axis ensures no risk is basically detected for the asset.

Based on what we have just discussed, **we propose the following form of the Υ indicator:**

$$\Upsilon = \mathcal{T} \times \frac{\mathcal{I}}{\pi} \times f_{cloud} \times \tau \tag{6.16}$$

where I is the orbital inclination of a projectile with respect to a non-equatorial target (i.e., the *relative* inclination). From [28]:

$$\mathcal{I} = 2 \arcsin \sqrt{\left[\sin\left(\frac{i - i_0}{2}\right)\right]^2 + \sin i_0 \sin i \left[\sin\left(\frac{\Omega - \Omega_0}{2}\right)\right]^2} \tag{6.17}$$

where i_0, i and Ω_0, Ω are the inclinations and longitudes of node of the asset (target) and the debris fragment (projectile), respectively. Not only does this expression account for the inclination between the target and projectile, but it also addresses collisions occurring at various relative velocities. This is ensured by the presence of the term $\Omega - \Omega_0$ in equation (6.17): if the target and projectile share the same *RAAN*, this difference amounts to zero, and the second term under the square brackets vanishes. On the other hand, if the two Ωs were supplementary angles, the term $\sin\left(\frac{\Omega-\Omega_0}{2}\right)$ would be at its maximum.

Emphasizing the benefits of utilizing the J_2 indicator, it is worth highlighting its advantage in providing a **preliminary assessment** of the short and medium-term risks associated with a cloud on a specific asset. This indicator can be calculated well in advance of obtaining more precise radar or optical tracking data for the fragments, and its primary purpose is not to make decisions but rather **to offer a valuable sense of alert**, aiding decision-makers in their overall risk assessment process.

6.3 An Algorithm for the J_2 indicator

An algorithm has been developed to calculate the J_2 indicator, as defined in equation (6.16), for various assets. Here, we will briefly outline the inputs and outputs of the algorithm. Additionally, in the following section, we will offer the reader examples illustrating the application of the algorithm.

6.3.1 Inputs and Outputs

The program takes as **inputs**:

- The cloud files generated by SDM [8], containing orbital elements of all fragments at a given epoch;
- The Δv files, containing the value of the Δv imparted to each fragment. These values are then averaged to estimate the values of T_b in Ashenberg's formulation (see (6.10)). For the same purpose, also the inclination of all fragments is averaged;
- The asset (satellite) orbital elements $(a_s, e_s, i_s, \Omega_s, \omega_s, M_s)$

And gives as **outputs**:

- The Υ value;
- A histogram plot showing the percentage of cloud fragments that could potentially interest the asset. These are defined as those fragments whose altitude is within the range $r_p \leq h_{fragment} \leq r_a$, where $r_p = a_s(1 - e_s)$ and $r_a = a_s(1 + e_s)$ are respectively the asset's perigee and the apogee.
- A 3D visual plot showcasing the potentially dangerous fragments and the asset's position at the fragmentation epoch, as well as its corresponding Keplerian orbit.

This algorithm can serve as a useful tool for assessing the potential hazards that may affect a particular asset, given a simulated fragmentation event. In the next section, we provide some interesting results.

6.4 Results

We considered the 450 km fragmentation introduced earlier in Sec. 5.3 and tested the algorithm on three different assets sharing the same orbital elements, except for the eccentricity:

$$(a_s, e_s, i_s, \Omega_s, \omega_s, M_s) = (7278\,\text{km}, e, 90^\circ, 0^\circ, 0^\circ, 0^\circ) \tag{6.18}$$

with $e_s \in [0.001, 0.01, 0.1]$.

Involved Fragments

It is interesting to take a look at the histogram plots we obtained, showing the percentage of fragments produced by the fragmentation which satisfy $r_p \leq h_{fragment} \leq r_a$, see Fig. 6.3. The most relevant aspect of these plots is the notable rise in the number of fragments involved, moving from the scenario with $e = 0.001$ to the one with

$e_s = 0.1$. As eccentricity increases, the apogee elevates and the perigee descends, thus our target is crossing a larger region of space leading to a higher effective number of fragments that could potentially affect it, thus leading to higher f_{cloud} values.

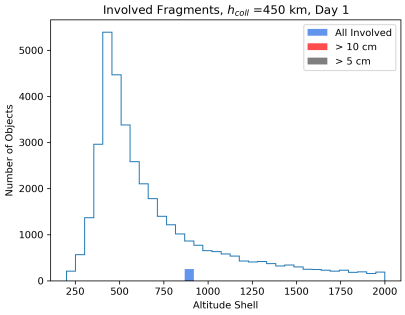

(a) Number of interested fragments on the asset (6.18) with $e = 0.001$.

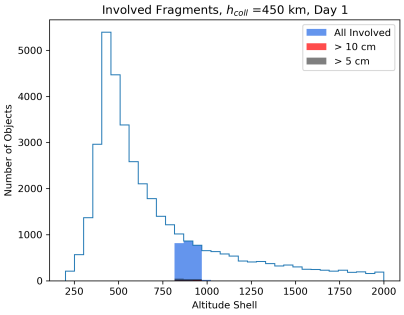

(b) Number of interested fragments on the asset (6.18) with $e = 0.01$.

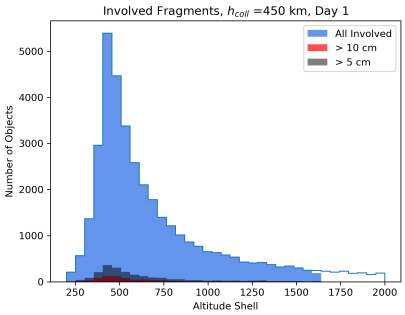

(c) Number of interested fragments on the asset (6.18) with $e = 0.1$.

Figure 6.3: Number of involved fragments (blue) per altitude shell for a 450 km collision, on an asset with orbital elements: $(a_s, e_s, i_s, \Omega_s, \omega_s, M_s) = (7278 \text{ km}, e, 90°, 0°, 0°, 0°)$. The number of fragments respectively greater than 5 cm (grey) and 10 cm (red) is also shown. The number of involved fragments increases with the eccentricity value e. The histograms refer to one day after the fragmentation epoch.

Yet, knowledge of the fragment count alone doesn't provide meaningful physical insights. Consider the extreme scenario of a Geostationary Earth Orbit (GEO) satellite, whose orbit is significantly larger than the entire distribution of fragments resulting from our 450 km fragmentation event. In this case, the asset remains secure since it spends no portion of its orbital period intersecting with the fragments; it occupies an entirely distinct orbit or, in other words, $\mathcal{T} = 0$ - see (6.16) for the definition $\mathcal{T}$ and Fig. 6.4b to get an immediate visual representation of what we just said. To compute the percentage of orbital period spent by a satellite in the region of interest, we computed the Φ function as defined in equation (3.6), which gives the fraction of orbital period spent in a given shell range with extremes r_{in} and r_{out}. In our algorithm, the region of interest is constituted of all the altitude shells the asset intersects over its orbit. In Figure 6.5 we offer a visual representation (computed as an output to our algorithm) of the interested fragments' evolution for fragmentation with $h_{frag} = 450\ km$ and for the asset at 900 km altitude. Four snapshots are shown, respectively at times $t_1 = 1, t_2 = 50, t_3 = 100$ and $T_b = 357$ days from the fragmentation epoch. It is interesting to note how, at T_b, the cloud appears to have completely spread. This is due to the J_2 effect, whose role is to randomize the fragments' perigee argument and longitude of node. The sinking of fragments is also evident from the significantly reduced number of points in 6.5c: the drag effect is prominent, the cloud being in LLEO.

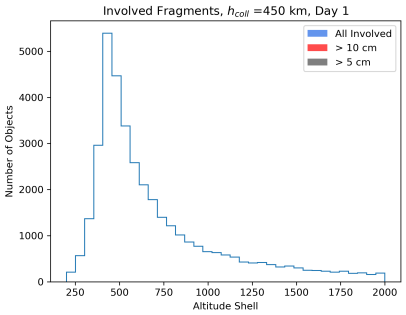

(a) Histogram showing the percentage of fragments involved.

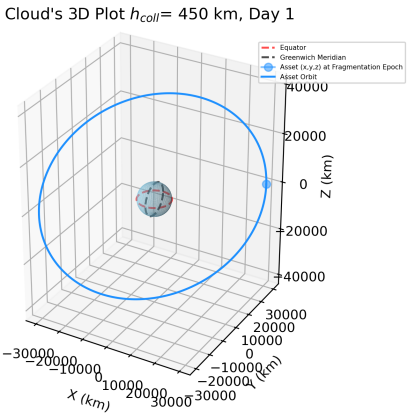

(b) 3D visualization plot for a geostationary asset.

Figure 6.4: Left: Number of involved fragments for the 450 km collision on a geostationary asset with orbital elements: $(a_s, e_s, i_s, \Omega_s, \omega_s, M_s) = (42378\ \text{km}, 0.001, 90°, 45°, 0°, 0°)$. All cloud fragments are involved. **Right**: 3D visual representation. A spherical Earth is shown in blue, together with the Greenwich meridian (black) and the equator (red). Basically, all fragments (grey) are found inside the satellite's orbit (light blue); however, the fraction of orbital period spent by the satellite among the interested altitude shells is null.

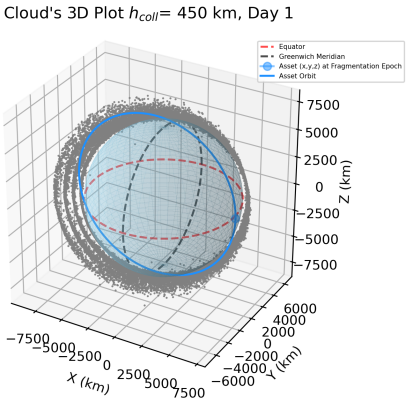

(a) Involved fragments position and satellite's orbit 1 Day after the fragmentation epoch.

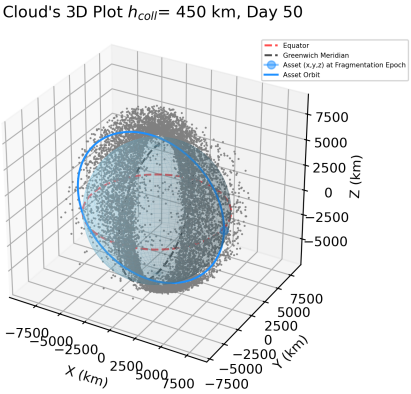

(b) Involved fragments position and satellite's orbit 50 Days after the fragmentation epoch.

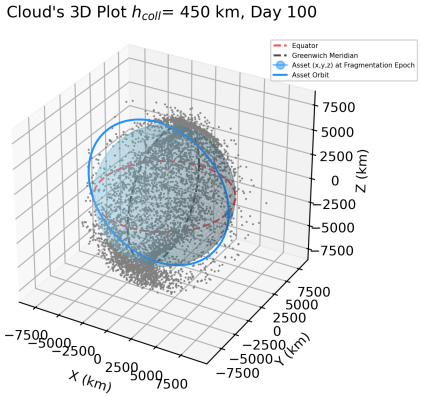

(c) Involved fragments position and satellite's orbit 100 Days after the fragmentation epoch.

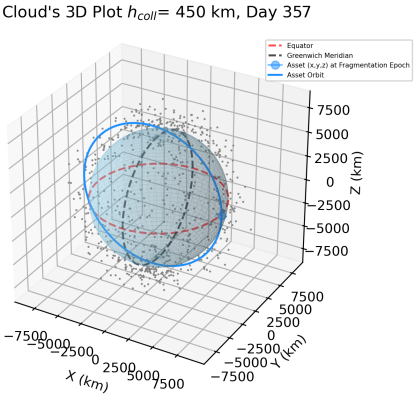

(d) Involved fragments position and satellite's orbit at $T_b = 357$ Days after the fragmentation epoch.

Figure 6.5: Evolution of the cloud's potentially hazardous fragments for the 450 km collision on an asset with orbital elements: $(a_s, e_s, i_s, \Omega_s, \omega_s, \mathcal{M}_s) = (7278\,\text{km}, 0.1, 90°, 0°, 0°, 0°)$. A spherical Earth is shown in blue, together with the Greenwich meridian (black) and the equator (red). All fragments (grey) are found inside the satellite's orbit (light blue).

6.4.1 Comparisons Among Various Assets and Fragmentation Cases

In order to validate and make sense of the obtained results, it is useful to compare the J_2 indicator values for different fragmentation altitudes and on assets with different orbits, i.e. characterized by different orbital elements.

In particular, we considered the following combinations:

- an asset with orbital elements: $(a_s, e_s, i_s, \Omega_s, \omega_s, M_s) = (h_s = 900\,\text{km}, e, 90°, 0°, 0°, 0°)$ - with $e = 0.001, 0.01, 0.1$ respectively - against the fragmentation cases with $h_{frag} = 450, 800, 1200\ km$;
- an asset with $(a_s, e_s, i_s, \Omega_s, \omega_s, M_s) = (h_s = 1700\,\text{km}, e, 90°, 0°, 0°, 0°)$ against the case with $h_{frag} = 1800\ km$;
- an asset with $(a_s, e_s, i_s, \Omega_s, \omega_s, M_s) = (h_s = 1300\,\text{km}, e, 90°, 0°, 0°, 0°)$ for the two fragmentation cases at $h_{frag} = 1200\ km$ and $h_{frag} = 1800\ km$, in order to probe the effect of a semi-major axis change on the J_2 indicator.

Moreover, as we shall see in presenting our comparisons, we also simulated two more fragmentation cases at an altitude of $h_{frag} = 800\ km$, with parent object inclinations of $i_p = 60°$ and $i_p = 85°$, in order to contrast them with the $h_{frag} = 800\ km$, $i_p = 80°$ case. Our results are shown in Figure 6.6. First, consider only the four solid-line cases on the top plot. **The indicator's value is seen to increase with increasing eccentricity** of the target asset. This is of course a consequence of the greater number of altitude shells - and therefore, of cloud debris - encountered by the asset along its orbit. It is also important to stress that Υ depends on the **relative satellite-fragmentation altitude**. For instance, for the asset at $h_s = 900$ km, the solid-blue line, corresponding to $h_{frag} = 800$ km is always *above* the green-solid line, representing the case for which $h_{frag} = 1200$ km. However, changing h_{sat} from 900 km to 1300 km, we can see in the second panel that the dashed-green line is always found above the green-solid one and it is actually always at the *same level or above* the solid-blue line of the previous panel. This is of course expected because, in the first case, the satellite orbiting at 900 km is "closer" (in terms of the semi-major axis) to the 800 km altitude shell and further from the 1200 km one. The opposite is true when we consider an asset with $h_{sat} = 1300$ km. In a similar way, it can be seen in the third panel, pertaining to the fragmentation at $h_{frag} = 1800$ km, that the $h_s = 1700$ km is above the $h_s = 1300$ km black-dashed line, the second having a higher relative altitude separation. What about the role of the debris cloud's inclination? This was tested by comparing three fragmentation events at an altitude of 800 km, all sharing the same characteristics as the ones presented in Sec. 5.3, but having different parent object's inclination values of $i_p = 60°, 80°, 85°$ respectively. The obtained results are showcased in the last plot of Fig. 6.6: it is clear that, among the three blue lines, the dotted one - corresponding to an average fragments' inclination of $\bar{i} \sim 85°$ - gives the highest Υ for all eccentricity values. According to equation 6.10, such fragmentation has a very high T_Ω, which makes it particularly hazardous to the considered asset, it having an inclination of 90°. This is exactly the behavior we tried to explain in section 6.2. Of course, this high risk is only found for assets sharing a specific geometry (for instance those with a similar high inclination value and in regions nearby), while satellites with lower inclinations will not show such high J_2 indicator values. Other interesting insights can be gained on the T_b value as a function of fragmentation altitude. Figure 6.7 visually shows that higher fragmentation altitudes are associated with longer spreading timescales, as expected. Please note once again that the T_b value is independent on the asset's orbital elements, as it only depends on the **PFO** orbital elements (especially the average inclination of fragments), and the Δv distribution. T_b values in 6.7 have been computed using the mean fragments' inclination and Δv values for all collisions presented in

Sec. 5.3. The former amounts to $\bar{i} = 80°$ for all cases, while the latter has a value of about $\overline{\Delta v} = 0.31$ km/s. It is clear that, depending on the collision characteristics, especially inclination and Δv, the plot in Fig. 6.7 would change. For instance, a lower $\bar{i}$ value yields lower T_b values, effectively translating the graph down the y-axis, see Fig. 6.7. It is worth noting that we have verified the correctness of our T_b computation, comparing our results with the ones (obtained with a slightly different Δv value) given in [29], Fig 3.

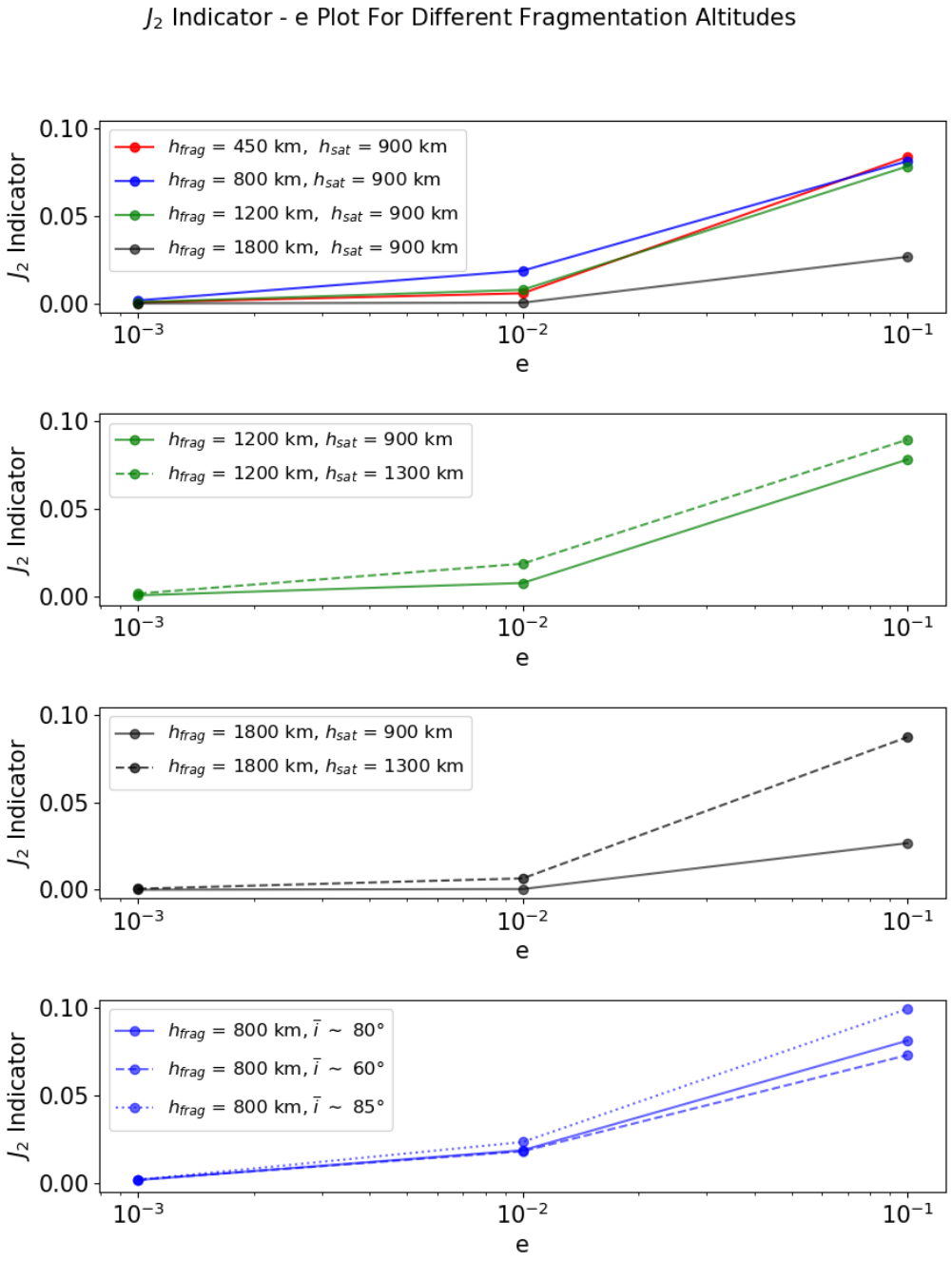

Figure 6.6: Top Panel: J_2 indicator values for an asset with $(a_s, e_s, i_s, \Omega_s, \omega_s, M_s) = (h_s = 900 \text{ km}, e, 90°, 0°, 0°, 0°)$ for all fragmentations in 5.3. **Second and Third Panel**: J_2 indicator values for an asset with $(a_s, e_s, i_s, \Omega_s, \omega_s, M_s) = (h_s = 1300 \text{ km}, e, 90°, 0°, 0°, 0°)$ and $h_{frag} = 1200, 1800$ respectively. **Bottom Panel**: J_2 indicator values for fragmentations happening at the same altitude of $h_{frag} = 800\ km$, and produced by parent objects with different inclinations, $i_p = 60°, 80°, 85°$ respectively. Please note that $e = 0.001, 0.01, 0.1$.

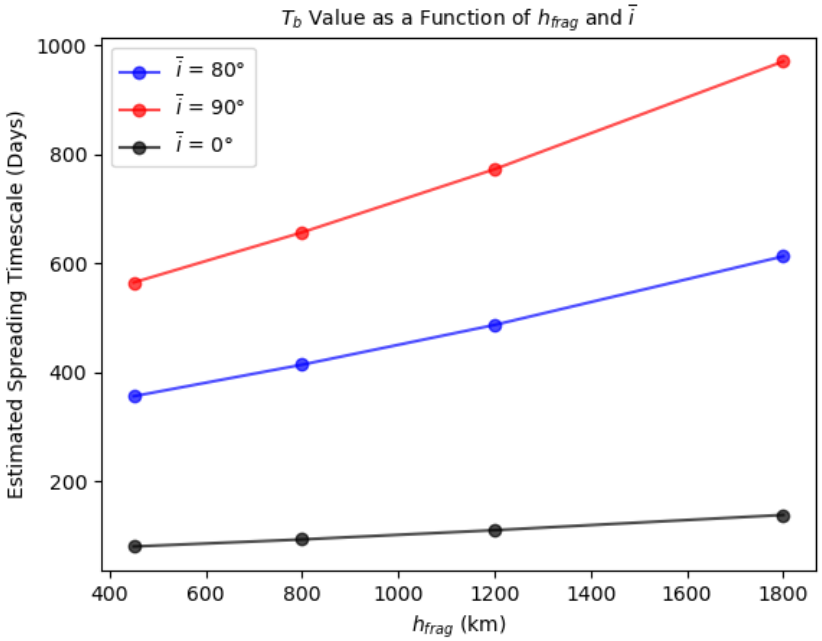

Figure 6.7: Cloud's spreading timescale (T_b values) as a function of h_{frag} and $\bar{i}$.

7

Conclusions and Future Works

This thesis work aimed at addressing two key questions related to the Space Surveillance and Tracking domain:

- *"Is there a way to quickly measure the short-term effects of an in-orbit fragmentation on a given sensor network?"*
- *"Are we able to give decision-makers a quick overview of the risk associated with given fragmentation on a given asset, at some time in the future?"*

To understand the meaning of the first question, imagine that a perfect surveillance network is in place. Then any fragment produced by a given fragmentation would be quickly tracked and catalogued, allowing it to pass its coordinates to the collision avoidance service in the SST system. Therefore, the risk posed by the fragmentation event on the controlled orbital assets would be minimized. On the other hand, a poorly performing space surveillance network would not be able to track most of the small fragments, thus breaking the chain of SST services, and not providing adequate information for the collision avoidance procedures. To give an answer to the first question, a **Fragmentation Environmental Index (FEI)** was originally devised in [1] to quickly assess whether a fragmentation event in Low-Earth Orbit is going to stress the capabilities of a given **surveillance network**. In [1] a very preliminary and simple characterization of the observing network was used. Our work aimed at improving the FEI by parametrizing the performances of typical optical and radar sensors, adopting specific weighting functions and quantifying the observability of the fragments as a function of their size and orbital regions. In particular, the optical and radar SNR **detection signatures** were used for the scope. For optical telescopes, we developed an **observability function** that considers the Angular Rate and size of the fragments. Fragments passing across the Field of View (FOV) at a lower altitude move faster. Hence, they are more difficult to observe and are therefore assigned a higher weight in the index computation. This insight suggests that optical sensors are more effective for monitoring the High LEO region, roughly above 1200 km of altitude. On the other hand, radars were considered to be better suited for probing the Low LEO and Medium LEO orbital regimes, the SNR_{radar} dropping quickly as a function of the fragments' range ($SNR_{radar} \propto \rho^{-4}$). To validate the new index, a number of tests

have been performed over synthetic fragmentation clouds generated with the NASA Breakup Model through the SDM software suite. The FEI was computed for fragmentations happening at different altitudes. Due to the reasons explained above, a radar network was assumed to be in place, able to probe altitudes up to 1200 km, while the optical network was assumed to observe higher altitudes, up to the LEO limit of 2000 km. The presented results showcased the capability of the index to catch the actual time evolution of the risk (as mentioned above, associated with the capability of our simulated network to observe the generated fragments) in the region of space interested by the fragmentation in the **short-medium** term. This quality makes it a **quick diagnostic tool** for **space debris mitigation**. The FEI can be deduced promptly upon the initial detection of the first fragments, even preceding subsequent observations that provide more accurate orbit determination. It is adaptable for simulations across various networks, enabling the assessment of their responsiveness to a given cloud. Consequently, it could also prove valuable for the purpose of **sensor tasking**.

To give an answer to the second question - thanks to an analysis based more on **orbital dynamics** considerations - we also considered the role of the J_2, i.e., the quadrupole term of the expansion of the geopotential in spherical harmonics, in shaping the evolution of a fragmentation cloud. We made use of this knowledge to introduce a novel indicator, called Υ, or "J_2 **indicator**", which aims at giving decision-makers a quick look at the overall risk given by the cloud as associated with a given asset. Υ depends on: the relative inclination $\mathcal{I}$ between the mean fragments inclination (considered as projectiles) and the inclination of the asset itself (the target); the percentage of fragments that could potentially interest the cloud, the cloud's spreading timescale and the amount of time $\mathcal{T}$ spent by the asset in the critical post-fragmentation regions. The J_2 indicator could serve as a rapid tool to inform decision-makers of **anticipated outcomes** from a given LEO fragmentation event.

Part of this thesis was presented orally during the **Second International Orbital Debris Conference** (IOC II) in Sugar Land (Houston, TX, USA), raising the interest of the SST experts attending the event. Future developments on the topic will aim at producing a cumulative index over a specific time span to directly classify and rank different fragmentation events on various regions of LEO, akin to the **Palermo Scale**used to evaluate the risk posed by Near Earth Objects.

Acknowledgments

I'm extremely grateful to Dr. Alessandro Rossi (IFAC-CNR) and Professor Francesco Marzari (University of Padova) for their invaluable support throughout the creation of this thesis, and for their professionalism: thank you for showing me how to critically approach a problem and break it down into smaller pieces, allowing me to consider simple possible solutions.

I would also like to extend my sincere thanks to Professor Dr. Thomas Schildknecht (Universität Bern): his comments have turned out to be very useful in that they indicated critical points regarding this work.

I will never forget the extraordinary opportunity I had to spend part of my academic career at the ESA's Near-Earth Objects Coordination Center. Here at ESRIN, I met some of the most inspiring people I have ever known. Their teachings, humility, and the coffee breaks we shared will forever hold a very special place in my heart. It was here that I truly understood what it means to be part of a Team, and how a Monte Carlo Simulation *actually* works!

Thanks to my friends, because they have always made me feel loved and taken care of. And thanks to my amazing family: in the vast array of "possible worlds", I am grateful to have ended up in yours. None of this would have ever been possible without you.

As this chapter is coming to an end, I would like to thank the city of Padova and its university for welcoming me when I was still a teenager, and for guiding me through its occasionally intricate yet always beautiful paths. In the end, they all converged to this point, which is exactly where I would like to be.

Luigi,

Frascati, 23/03/2024

References

[1] A. Rossi, E. Vellutini, E. Alessi, G. Schettino, V. Ruch, and J. Dolado Perez, "Environmental index for fragmentation impact and environment evolution analysis," *Journal of Space Safety Engineering*, vol. 9, no. 2, pp. 269–273, Jun. 2022. [Online]. Available: https://linkinghub.elsevier.com/retrieve/pii/S2468896722000180

[2] J. Shell, "Optimizing Orbital Debris Monitoring with Optical Telescopes," in *Proceedings of the Advanced Maui Optical and Space Surveillance Technologies Conference*, Sep. 2010, p. 18. [Online]. Available: https://amostech.com/TechnicalPapers/2010/Systems/Shell.pdf

[3] R. Jehn, "Dispersion of Debris Cloud from In-Orbit Fragmentation Events," *Journal of Spacecraft and Rockets (ISSN 0022-4650)*, vol. vol. 31, no. 6, pp. 1044–1049, Sep. 1990. [Online]. Available: https://ui.adsabs.harvard.edu/abs/1990dres.iafc.....J/abstract

[4] F. Letizia, C. Colombo, H. Lewis, and C. McInnes, "Debris cloud evolution in Low Earth Orbit," in *Proceedings of the International Astronautical Congress, IAC*, vol. 4, Sep. 2013. [Online]. Available: https://www.researchgate.net/publication/257603878_Debris_cloud_evolution_in_Low_Earth_Orbit

[5] H. Klinkrad, *Space debris: models and risk analysis*, ser. Springer-Praxis books in astronautical engineering. Berlin ; New York : Chichester, UK: Springer ; Published in association with Praxis Pub, 2006. [Online]. Available: https://link.springer.com/book/10.1007/3-540-37674-7

[6] D. J. Kessler and B. G. Cour-Palais, "Collision frequency of artificial satellites: The creation of a debris belt," *Journal of Geophysical Research: Space Physics*, vol. 83, no. A6, pp. 2637–2646, Jun. 1978. [Online]. Available: https://agupubs.onlinelibrary.wiley.com/doi/10.1029/JA083iA06p02637

[7] D. J. Kessler, "Collisional cascading: The limits of population growth in low earth orbit," *Advances in Space Research*, vol. 11, no. 12, pp. 63–66, Jan. 1991. [Online]. Available: https://linkinghub.elsevier.com/retrieve/pii/027311779190543S

[8] A. Rossi, G. Valsecchi, and E. Alessi, "The Criticality of Spacecraft Index," *Advances in Space Research*, vol. 56, no. 3, pp. 449–460, Aug. 2015. [Online]. Available: https://linkinghub.elsevier.com/retrieve/pii/S0273117715001556

[9] C. Bombardelli, E. Alessi, A. Rossi, and G. Valsecchi, "Environmental effect of space debris repositioning," *Advances in Space Research*, vol. 60, no. 1, pp. 28–37, Jul. 2017. [Online]. Available: https://linkinghub.elsevier.com/retrieve/pii/S0273117717302491

[10] A. Rossi, L. Anselmo, C. Pardini, R. Jehn, and G. Valsecchi, "The new space debris mitigation (SDM 4.0) long term evolution code," in *Proceedings of the Fifth European Conference on Space Debris, ESA SP-672, CD-ROM, ESA Communication Production Office, Noordwijk, The Netherlands*, 2009. [Online]. Available: https://conference.sdo.esoc.esa.int/proceedings/sdc5/paper/48/SDC5-paper48.pdf

[11] N. L. Johnson, P. H. Krisko, J. C. Liou, and P. D. Anz-Meador, "NASA's new breakup model of evolve 4.0," *Advances in Space Research*, vol. 28, no. 9, pp. 1377–1384, Jan. 2001. [Online]. Available: https://www.sciencedirect.com/science/article/pii/S0273117701004239

[12] A. Rossi, E. M. Alessi, G. Valsecchi, H. Lewis, J. Radtke, C. Bombardelli, and B. Virgili, "A Quantitative Evaluation of the Environmental Impact of the Mega Constellations," Apr. 2017. [Online]. Available: https://www.researchgate.net/publication/316441394_A_Quantitative_Evaluation_of_the_Environmental_Impact_of_the_Mega_Constellations

[13] A. Milani and G. Gronchi, *Theory of Orbit Determination*, 1st ed. Cambridge University Press, Nov. 2009. [Online]. Available: https://www.cambridge.org/core/product/identifier/9781139175371/type/book

[14] T. Schildknecht, "Optical surveys for space debris," *The Astronomy and Astrophysics Review*, vol. 14, no. 1, pp. 41–111, Jan. 2007. [Online]. Available: http://link.springer.com/10.1007/s00159-006-0003-9

[15] T. Schildknecht, T. Flohrer, and A. Vananti, "Optical Surveys for Space Debris in MEO–Simulations and First Results," in *Proceedings of the 60th International Astronautical Congress, Daejeon/Republic of Korea*, vol. 3, Jan. 2009. [Online]. Available: https://www.researchgate.net/publication/259260646_Optical_Surveys_for_Space_Debris_in_MEO--Simulations_and_First_Results

[16] V. Yurasov and V. Shargorodskiy, "Features of space debris survey in LEO utilizing optical sensors," vol. 672, Jan. 2009. [Online]. Available: https://conference.sdo.esoc.esa.int/proceedings/sdc5/paper/7/SDC5-paper7.pdf

[17] D. Pollacco, I. Skillen, A. Cameron, D. Christian, C. Hellier, J. Irwin, T. Lister, R. Street, R. West, D. Anderson, W. Clarkson, H. Deeg, B. Enoch, A. Evans, A. Fitzsimmons, C. Haswell, S. Hodgkin, K. Horne, S. Kane, F. Keenan, P. Maxted, A. Norton, J. Osborne, N. Parley, R. Ryans, B. Smalley, P. Wheatley, and D. Wilson, "The WASP Project and the SuperWASP Cameras," *Publications of the Astronomical Society of the Pacific*, vol. 118, no. 848, pp. 1407–1418, Oct. 2006. [Online]. Available: http://iopscience.iop.org/article/10.1086/508556

[18] G. Beskin, S. Bondar, S. Karpov, V. Plokhotnichenko, A. Guarnieri, C. Bartolini, G. Greco, A. Piccioni, and A. Shearer, "From TORTORA to MegaTORTORA—Results and Prospects of Search for Fast Optical Transients," *Advances in Astronomy*, vol. 2010, pp. 1–9, 2010. [Online]. Available: http://www.hindawi.com/journals/aa/2010/171569/

[19] K. Małek, T. Batsch, H. Czyrkowski, M. Ćwiok, R. Dąbrowski, W. Dominik, G. Kasprowicz, A. Majcher, A. Majczyna, L. Mankiewicz, K. Nawrocki, R. Pietrzak, L. W. Piotrowski, M. Ptasińska, M. Siudek, M. Sokołowski, J. Użycki, P. Wawer, R. Wawrzaszek, G. Wrochna, M. Zaremba, and A. F. Żarnecki, ""Pi of the Sky" Detector," *Advances in Astronomy*, vol. 2010, pp. 1–9, 2010. [Online]. Available: http://www.hindawi.com/journals/aa/2010/194946/

[20] M. Mulrooney, M. Matney, M. Hejduk, and E. Barker, "An Investigation of Global Albedo Values," Jan. 2008. [Online]. Available: https://www.researchgate.net/publication/241291746_An_Investigation_of_Global_Albedo_Values

[21] R. Pellegrini, P. Gregori, F. Cerutti, L. Dimare, F. Bernardi, D. Bracali Cioci, and E. Vellutini, "SUTED4L –Study for the application of the Flyeye Telescope to the Survey of the High-LEO orbital region," in *2nd NEO and Debris Detection Conference*. Darmstadt, Germany: ESA Space Safety Programme Office, Jan. 2023. [Online]. Available: https://conference.sdo.esoc.esa.int/proceedings/neosst2/paper/30/NEOSST2-paper30.pdf

[22] A. Crumey, "Human contrast threshold and astronomical visibility," *Monthly Notices of the Royal Astronomical Society*, vol. 442, no. 3, pp. 2600–2619, Aug. 2014. [Online]. Available: http://academic.oup.com/mnras/article/442/3/2600/1052389/Human-contrast-threshold-and-astronomical

[23] G. Mie, "Beiträge zur Optik trüber Medien, speziell kolloidaler Metallösungen," *Annalen der Physik*, vol. 330, no. 3, pp. 377–445, Jan. 1908. [Online]. Available: https://onlinelibrary.wiley.com/doi/10.1002/andp.19083300302

[24] H. Klinkrad, J. Bendisch, K. Bunte, H. Krag, H. Sdunnus, and P. Wegener, "The MASTER-99 space debris and meteoroid environment model," *Advances in Space Research*, vol. 28, no. 9, pp. 1355–1366, Jan. 2001. [Online]. Available: https://linkinghub.elsevier.com/retrieve/pii/S0273117701004161

[25] V. A. Chobotov, "Dynamics of orbiting debris clouds and the resulting collision hazard to spacecraft," *Journal of the British Interplanetary Society*, vol. 43, pp. 187–194, 1990. [Online]. Available: https://api.semanticscholar.org/CorpusID:124253409

[26] J. Ashenberg, "Formulas for the phase characteristics in the problem of low-earth-orbital debris," *Journal of Spacecraft and Rockets*, vol. 31, no. 6, pp. 1044–1049, Nov. 1994. [Online]. Available: https://arc.aiaa.org/doi/10.2514/3.26556

[27] J. Slotten, "EXAMINATION OF DEBRIS CLOUD DENSITY RESULTING FROM PRECESSION OF ARGUMENT OF PERIGEE DUE TO J2 EFFECT," Apr. 2017. [Online]. Available: htthttps://conference.sdo.esoc.esa.int/proceedings/sdc7/paper/530

[28] R. B. Southworth and G. S. Hawkins, "Statistics of meteor streams," *Smithsonian Contributions to Astrophysics*, vol. 7, pp. 261–285, Jan. 1963, aDS Bibcode: 1963SCoA....7..261S. [Online]. Available: https://ui.adsabs.harvard.edu/abs/1963SCoA....7..261S

[29] F. Letizia, C. Colombo, and H. G. Lewis, "Analytical Model for the Propagation of Small-Debris-Object Clouds After Fragmentations," *Journal of Guidance, Control, and Dynamics*, vol. 38, no. 8, pp. 1478–1491, Aug. 2015. [Online]. Available: https://arc.aiaa.org/doi/10.2514/1.G000695